Structural acoustic controlled active micro-perforated panel absorber for improving wide-band low frequency sound absorption

Xiyue Ma[1, 2)], Daniil Yurchenko[3)], Kean Chen[1, 2)], Lei Wang[4)], Yang Liu[1, 2)], Kai Yang[5)*]

1) *School of Marine Science and Technology, Northwestern Polytechnical University, Xi'an 710072, P. R. China*
2) *Key Laboratory of Ocean Acoustics and Sensing (Northwestern Polytechnical University), Ministry of Industry and Information Technology*
3) *Institute of Sound and Vibration Research, University of Southampton, SO17 1BJ, UK*
4) *School of Science, Xi'an University of Architecture and Technology, Xi'an 710055, P. R. China*
5) *School of Aerospace Engineering, Huazhong University of Science and Technology, Wuhan 430074, P. R. China*

*Corresponding author. E-mail address: kaiyang@hust.edu.cn (Kai Yang)

Abstract: This paper investigates the performance of the structural acoustic controlled active micro-perforated panel absorber (SAC-AMPPA), which can achieve wide-band perfect low frequency sound absorption (absorption coefficient is close to 1). The SAC-AMPPA applies point force-controlled backing panel to actively improve the low-frequency sound absorption of the MPPA with the purpose of saving space to suit it better for applications. The theoretical model of the SAC-AMPPA is firstly established using the modal analysis approach. Influence of structure size and point force position on sound absorption performance is explored. Then, the experimental tests were performed to validate the theoretical modeling and findings. Finally, the physical mechanisms of active control are analyzed in detail and some physical insights are summarized. Simplified error sensing strategy for small sized SAC-AMPPA is also constructed. Results obtained show that the preconditions of the point force locating at the center of the backing panel or relatively small sized SAC-AMPPA can guarantee less cavity modes being excited and achieving perfect sound absorption in a very wide controllable bandwidth. The main reason of this lies in the key findings, i.e., except for the $(0,0,n)$ mode, other cavity modes excited by the backing panel cannot contribute to the improvement of low-frequency sound absorption below their resonant frequencies. They radiate sound energy towards the outside of SAC-AMPPA and play a negative role above their resonant frequencies. Provided a uniform cavity sound field is guaranteed in controlled condition, the sound pressure release (PR) and impedance matching (IM) strategies can be used to conveniently construct error sensing

strategy of the SAC-AMPPA.

Keywords: micro-perforated panel absorber, low frequency sound absorption, active control, sound absorption mechanism, error sensing strategy

1. Introduction

Micro-perforated panel (MPP) has been widely used as a classical type of efficient sound absorption materials due to the properties of light, fiberless, and highly efficient sound absorption performance [1-2]. The MPP absorber (MPPA) is commonly used form in practice, in which the MPP is placed in front of a rigid backing wall [3]. The shallow air cavity can generate resonance, which increases the particle velocity through the holes to effectively dissipate the acoustical energy and highly improves the sound absorption efficiency.

The effective absorption bandwidth for the MPPA with specific structural parameters (sound absorption coefficient greater than 0.5) is limited around its resonant frequency [3]. Many approaches are proposed to broaden the effective absorption bandwidth in mid and high frequency range (above 500Hz). Such as series type MPPA with multiple MPP layers in the cavity [4-9] or a parallel type absorber with multiple MPPAs arranging in parallel [10-11], broaden the absorption bandwidth by combining different effective bandwidth together. Other method is improving the design of the MPPA to enhance the vibro-acoustic coupling effect between the MPP and the cavity [12-22], such as MPPA with irregular-shaped cavity [12-13]. Some passive and active approaches are also developed for improving low frequency sound absorption (lower than 500Hz). The passive method mainly introduces resonant structure to improve the sound absorption in a narrow bandwidth around the resonant frequency [23-26]. The new type of MPPA with corrugated MPP can also broaden the low frequency bandwidth [27]. However, the active method can achieve the broadband improvement of low frequency sound absorption [28]. Such method is also attractive in the field of mechanical metamaterials, such as constructing active meta-layer or metasurface for absorption and tunable ray steering of flexural wave [29-30] and active metamaterials with odd micropolar elasticity [31]. Cobo et al. [32-34] proposed a hybrid system that used a piston source to actively improve the low frequency sound absorption for the small sized MPPA with plane wave excitation. Two control strategies are developed, i.e., impedance matching (IM) and pressure release (PR) strategy, which indirectly adjusts the surface impedance of the MPPA to match that of the air medium. Ma et al. further expanded this work to large sized active MPPA, which demonstrated the feasibility of this approach in large sized case [35].

The cone loudspeaker is used as the control element to realize the piston type source in Ref [32-35]. There is another way to implement the active MPPA, which uses a point force-controlled backing panel as the control source to form the SAC-AMPPA. The low frequency

sound absorption can also be improved by using active structure acoustic control approach to adjust the surface impedance of the active MPPA. The piezoelectric excitation or small sized shaker [36] placed in the cavity can excite the backing panel, or the planar loudspeaker can directly be used for achieving the point force-controlled plate. The thickness of the whole system becomes thinner, and the size of the active element can also be extended by using the large sized MPP and backing panel. Therefore, the SAC-AMPPA can be an effective supplementary approaching for meeting the requirements of ultrathin and large area sound absorption layer. It can be used to construct active acoustic liner or its absorbed sound energy can be harvested to generate electricity [37-39]. Ma et al. has carried out a preliminary study on the SAC-AMPPA in which an error sensing strategy is constructed by using a limited number of acoustic vector sensors to measure the surface average impedance ratio [40]. However, the performance of active sound absorption, the influence of the point force arrangement on control effect and physical mechanism of active control are not yet explored, which is of great importance for understanding physical nature of the SAC-AMPPA and carrying out structural optimization. Due to the complex vibration of the backing panel, the sound field in the cavity becomes complex and cannot longer be treated as the superposition of the incident and reflected plane wave as in Ref [32-35]. The corresponding physical nature will be different from the existing results. Hence, the purpose of this research is to fill these gaps, which is of great significance for engineering implementation of such a technic.

The MPP is considered as an elastic plate and modal analysis approach [41-44] wass adapted to the SAC-AMPPA model in Ref [40]. The gain of sound absorption induced by MPP resonances in the low frequency range below the HC resonance is tiny for the MPPA [41]. The reason is that although the MPP resonances can marginally adjust the acoustic resistance of the MPPA towards that of the air, the large low-frequency stiffness-like reactance of the cavity mitigated the gain in absorption. To this end, it is predictable that the adjustment of the surface impedance of the SAC-AMPPA should be mainly induced by the variation of cavity sound field and the highly improved particle velocity in the micro-pore of the MPP in controlled condition. Thus, the MPP is considered as rigid in this study, which allows the attention being concentrated on exploring the mechanism of sound absorption improvement induced by the main cause of the backing panel vibration induced-cavity sound field variation. The influence of the secondary factor of MPP vibration to the sound absorption improvement in the control process is left for ongoing research. Then, the simplified modal analysis approach, similar to Ref [35] is used to establish the theoretical model.

The remainder of this paper is organized as follows. The theoretical model is established in Sec.2. The control performance is analyzed in Sec.3. Experimental validation is carried out

in Sec.4. An in-depth investigation on the control mechanism is presented in Sec.5. Simplified error sensing strategy is constructed in Sec.6. Conclusions are summarized in Sect.7.

2. Theory

2.1. Vibro-acoustic response of the SAC-AMPPA

Figure 1 presents the schematic diagram (a) and the modeling sketch (b) of the SAC-AMPPA. The rectangular SAC-AMPPA is placed at the end of a duct and a point force is assumed for simplicity. The surface impedance of the MPPA can be adjusted by actively controlling the vibration of the backing panel to vary the cavity sound field (so called active structure acoustic control approach). The low frequency sound absorption can be significantly improved when the appropriate control force is applied to adjust the surface impedance close to the characteristic impedance of air.

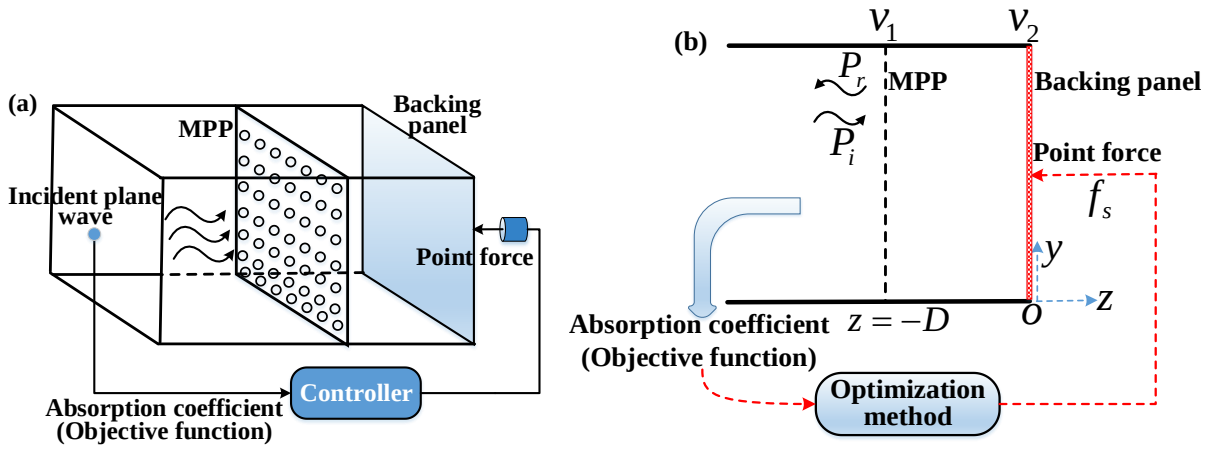

Fig.1. The SAC-AMPPA: (a) schematic diagram, (b) modeling sketch

The sound pressure in the cavity is $P_c(x,y,z,t)$ satisfies the homogeneous wave equation when there is no excitation source in the cavity [35],

$$\nabla^2 P_c(x,y,z,t) - \frac{1}{c_0^2}\frac{\partial P_c(x,y,z,t)}{\partial t^2} = 0 \tag{1}$$

where c_0 is the sound speed in air. The normal particle velocities on the surface of the MPP and backing panel in the cavity satisfy the following continuity boundary conditions, i.e., $\partial P_c/\partial \mathbf{n} = j\omega\rho_0 v_1(x,y)$ ($\mathbf{n}$ towards the outside of the MPP) and $\partial P_c/\partial \mathbf{n} = -j\omega\rho_0 v_2(x,y)$ ($\mathbf{n}$ towards the outside of the backing panel). $v_1(x,y)$ and $v_2(x,y)$ are the normal velocities on the surface of MPP and backing panel, ρ_0 is the density of the air. $P_c(x,y,z,t)$ can be expressed as superposition of a series of cavity modes,

$$P_c(x,y,z,t)=\sum_{u=0}^{U}\sum_{w=0}^{W}\sum_{m=0}^{M}P_{uwm}(t)\psi_{uwm}(x,y,z) \tag{2}$$

where $P_{uwm}(t)$ is the modal amplitude of the (u,w,m) -th mode, $\psi_{uwm}(x,y,z)$ is the mode shape function of the cavity with rigid boundary, $\psi_{uwm}(x,y,z)=\cos(\frac{u\pi x}{a})\cos(\frac{w\pi y}{b})\cdot\cos(\frac{m\pi z}{D})$, a and b are the length and width of the SAC-AMPPA, and D is the cavity depth. Applying the Green's second formula and orthogonality of the mode shape functions yields the equation that the modal amplitude $P_{uwm}(\omega)$ satisfies,

$$M_{uwm}(\omega^2+2j\xi_{uwm}\omega_{uwm}\omega-\omega_{uwm}^2)P_{uwm}(\omega)=-(-1)^m j\omega\rho_0c_0^2\int_0^a\int_0^b v_1(x,y)\varphi_{uw}(x,y)\mathrm{d}x\mathrm{d}y + j\omega\rho_0c_0^2\int_0^a\int_0^b v_2(x,y)\varphi_{uw}(x,y)\mathrm{d}x\mathrm{d}y, \tag{3}$$

where ω_{uwm} and ξ_{uwm} are the resonant frequency and modal damping ratio of the (u,w,m) -th mode, $M_{uwm}=\iiint_V\psi_{uwm}(x,y,z)^2\mathrm{d}V$ is the generalized modal mass, $\varphi_{uw}(x,y)$ is the mode shape function of the cross-section in the duct, $\varphi_{uw}(x,y)=\cos(\frac{u\pi x}{a})\cos(\frac{w\pi y}{b})$.

According to Eq. (3), the modal amplitude $P_{uwm}(\omega)$ can be expressed as,

$$P_{uwm}(\omega)=-\frac{(-1)^m j\omega\rho_0c_0^2\int_0^a\int_0^b v_1(x,y)\varphi_{uw}(x,y)\mathrm{d}x\mathrm{d}y}{M_{uwm}(\omega^2+2j\xi_{uwm}\omega_{uwm}\omega-\omega_{uwm}^2)}+\frac{j\omega\rho_0c_0^2\int_0^a\int_0^b v_2(x,y)\varphi_{uw}(x,y)\mathrm{d}x\mathrm{d}y}{M_{uwm}(\omega^2+2j\xi_{uwm}\omega_{uwm}\omega-\omega_{uwm}^2)} \tag{4}$$

The sound energy absorbed by the SAC-AMPPA is a function of the control force. Accordingly, the reflected and total sound pressures on the incident side are also dependent on the control force. The acoustic velocity potential $\Phi_r(x,y,z,\omega)$ of the reflected plane wave can be expressed as [10],

$$\Phi_r(x,y,z,\omega)=\sum_{u=0}^{U}\sum_{w=0}^{W}R_{uw}e^{\mu^{uw}z}\varphi_{uw}(x,y), \tag{5}$$

where $\mu^{uw}=\sqrt{(\frac{u\pi}{a})^2+(\frac{w\pi}{b})^2-(\frac{\omega}{c_0})^2}$. The coefficient R_{uw} depends on the continuity boundary condition at the incident side ($z=-D$),

$$\left(\frac{\partial \Phi_i}{\partial z}+\frac{\partial \Phi_r}{\partial z}\right)\Big|_{z=-D}=v_1(x,y), \tag{6}$$

where $\Phi_i=-\frac{p_0}{\mathrm{j}\omega\rho_0}e^{-\mathrm{j}k_0 z}$ is acoustic velocity potential of the incident plane wave, p_0 is the amplitude of the incident sound pressure, $k_0=\omega/c_0$ is the wave number. Substituting Eq. (5) into Eq. (6) and applying the orthogonality of modal functions yield the expression of the coefficient R_{uw}, which can be referenced in Ref [35]. Then, the reflected sound pressure P_r at the surface of the SAC-AMPPA ($z=-D$) can be expressed as,

$$P_r(x,y)=-\rho_0\frac{\partial \Phi_r}{\partial t}|_{z=-D}=\sum_{u=0}^{U}\sum_{w=0}^{W}\frac{Z_{uw}^r}{\beta_{uw}}\left[\int_0^a\int_0^b v_1(x,y)\varphi_{uw}(x,y)\mathrm{d}x\mathrm{d}y\right]\varphi_{uw}(x,y)+\frac{jp_0k_0ab\mathrm{e}^{\mathrm{j}k_0D}}{\mu^{00}\beta^{00}}, \tag{7}$$

where $Z_{uw}^r=\frac{-j\omega\rho_0}{\mu^{uw}}$, $\beta^{uw}=\int_0^a\int_0^b\varphi_{uw}(x,y)^2\mathrm{d}x\mathrm{d}y$.

The surface velocity of the MPP $v_1(x,y)$ can be considered as a distributed particle velocity, spatially averaged over each aperture cell adjacent to the holes [35],

$$v_1(x,y)=\sigma\frac{P-P_{c,D}}{z_0}, \tag{8}$$

where P is the total sound pressure on the incident side ($z=-D$), $P=P_i+P_r$. $P_i=p_0\mathrm{e}^{\mathrm{j}k_0D}$ is the incident sound pressure. $P_{c,D}(x,y)$ is the sound pressure at $z=-D$ in the cavity. σ is the porosity of the MPP. z_0 is the acoustic impedance of each hole for the MPP, which is mainly dependent on the diameter of the holes d_h and thickness of the MPP t_h. Its expression can be referenced in Ref [35]. Substituting Eq. (2) and Eq. (7) into Eq. (8), and applying the orthogonality of mode shape functions yield the expression that $v_1(x,y)$ satisfies,

$$\int_0^a\int_0^b v_1(x,y)\varphi_{uw}(x,y)\mathrm{d}x\mathrm{d}y=A_{uw}\int_0^a\int_0^b v_2(x,y)\varphi_{uw}(x,y)\mathrm{d}x\mathrm{d}y+B_{uw}^1\int_0^a\int_0^b\varphi_{uw}(x,y)\mathrm{d}x\mathrm{d}y, \tag{9}$$

where A_{uw} and B_{uw}^1 can be expressed as,

$$A_{uw}=[1-\frac{\sigma}{z_0}Z_{uw}^r-\frac{\sigma}{z_0}\sum_{m=0}^{M}\frac{j\omega\rho_0c_0^2\beta^{uw}}{M_{uwm}(\omega^2+2j\xi_{uwm}\omega_{uwm}\omega-\omega_{uwm}^2)}]^{-1}$$

$$\cdot[-\frac{\sigma}{z_0}\sum_{m=0}^{M}\frac{(-1)^m\, j\omega\rho_0 c_0^2\beta^{uw}}{M_{uwm}(\omega^2+2j\xi_{uwm}\omega_{uwm}\omega-\omega_{uwm}^2)}], \tag{10}$$

$$B_{uw}^1=[1-\frac{\sigma}{z_0}Z_{uw}^r-\frac{\sigma}{z_0}\sum_{m=0}^{M}\frac{j\omega\rho_0 c_0^2\beta^{uw}}{M_{uwm}(\omega^2+2j\xi_{uwm}\omega_{uwm}\omega-\omega_{uwm}^2)}]^{-1}[\frac{\sigma p_0 \mathrm{e}^{jk_0D}}{z_0}+\frac{j\sigma p_0 k_0 ab\mathrm{e}^{\mathrm{j}k_0D}}{z_0\mu^{00}\beta^{00}}] \tag{11}$$

Based on the modal superposition theory, the vibration displacement of the backing panel $w_2(x,y,t)$ can be expressed as the superposition of a series of panel modes,

$$w_2(x,y,t)=\sum_{s=1}^{S}\sum_{n=1}^{N}B_{sn}\phi_s(x)\varphi_n(y), \tag{12}$$

where B_{sn} is the amplitude of the (s,n)-th mode, $\phi_s(x)\varphi_n(y)=\sin(s\pi x/a)\sin(n\pi y/b)$ is the mode shape function of the backing panel with simply supported boundary condition, S and N are the upper limit numbers of the panel mode.

Under the excitation of the cavity sound pressure $P_c(x,y,0)$ and point force f_c, the displacement of the backing panel satisfies the wave equation as,

$$D_2(\frac{\partial^4 w_2}{\partial x^4}+2\frac{\partial^4 w_2}{\partial x^2\partial y^2}+\frac{\partial^4 w_2}{\partial y^4})+\rho_2 h_2\frac{\partial^2 w_2}{\partial t^2}=P_c(x,y,0)+f_c, \tag{13}$$

where D_2, ρ_2 and h_2 are the bending stiffness, density and thickness of the backing panel, respectively. $f_c=F_c\delta(x-x_c,y-y_c)$, in which F_c is the amplitude of the point force and (x_c,y_c) is its coordinate position. Substituting Eq. (12) into Eq. (13), multiplying $\phi_s(x)\varphi_n(y)$ on both sides of Eq. (13) and applying the orthogonality of the mode shape functions yield the equation that the modal amplitude B_{sn} satisfies,

$$B_{sn}\alpha_{sn}Z_{sn}=\int_0^a\int_0^b P_c(x,y,0)\phi_s(x)\varphi_n(y)\mathrm{d}x\mathrm{d}y+F_cQ_{sn}, \tag{14}$$

where $\alpha_{sn}=\int_0^a\int_0^b\phi_s(x)^2\varphi_n(y)^2\mathrm{d}x\mathrm{d}y=ab/4$, $Z_{sn}=\rho_2h_2(\omega_{sn}^2+2j\xi_{sn}\omega_{sn}\omega-\omega^2)$, Q_{sn} is the generalized secondary modal force, $Q_{sn}=\phi_s(x_c)\varphi_n(y_c)$. Further substituting Eq. (4) and Eq. (9) into Eq. (14) yields the following equation,

$$B_{sn}\alpha_{sn}Z_{sn}=\sum_{u=0}^{U}\sum_{w=0}^{W}\sum_{m=0}^{M}\frac{C_{uwm}\int_0^a\int_0^b v_2(x,y)\varphi_{uw}(x,y)\mathrm{d}x\mathrm{d}y}{M_{uwm}(\omega^2+2j\xi_{uwm}\omega_{uwm}\omega-\omega_{uwm}^2)}\gamma_{sn}^{uw}+D_{sn}+F_cQ_{sn}, \tag{15}$$

where the coupling coefficient $\gamma_{sn}^{uw} = \int_0^a \int_0^b \cos(\frac{u\pi x}{a})\cos(\frac{w\pi y}{b})\sin(\frac{s\pi x}{a})\sin(\frac{n\pi y}{b})\mathrm{d}x\mathrm{d}y$,

$C_{uwm} = j\omega\rho_0 c_0^2 - (-1)^m j\omega\rho_0 c_0^2 A_{uw}$, $D_{sn} = -\sum_{m=0}^{M} \frac{(-1)^m j\omega\rho_0 c_0^2 B_{00}^1 ab}{M_{00m}(\omega^2 + 2j\xi_{00m}\omega_{00m}\omega - \omega_{00m}^2)}\gamma_{sn}^{00}$. The velocity of the backing panel $v_2(x,y)$ in Eq. (15) can be further modal expanded, then, Eq. (15) can be re-expressed as,

$$B_{sn}\alpha_{sn}Z_{sn} - \sum_{u=0}^{U}\sum_{w=0}^{W}\sum_{m=0}^{M} \frac{C_{uwm}\sum_{s'=1}^{S}\sum_{n'=1}^{N} j\omega B_{s'n'}\gamma_{s'n'}^{uw}}{M_{uwm}(\omega^2 + 2j\xi_{uwm}\omega_{uwm}\omega - \omega_{uwm}^2)}\gamma_{sn}^{uw} = D_{sn} + F_c Q_{sn}\,. \tag{16}$$

According to Eq. (16), the column vector $\mathbf{B}$ of $S \times N$ modal amplitudes of the backing panel satisfies the matrix equation as,

$$\mathbf{EB} = \mathbf{D} + F_c\mathbf{Q}, \tag{17}$$

where $\mathbf{B} = [B_{11},...B_{sn},...B_{SN}]^T$, $\mathbf{D} = [D_{11},...D_{sn},...D_{SN}]^T$ and $\mathbf{Q} = [Q_{11},...Q_{sn},...Q_{SN}]^T$. $\mathbf{E}$ is the $(S \times N) \times (S \times N)$ coupling coefficient matrix, whose $(sn, s'n')$ element is expressed as,

$$E(sn, s'n') = \alpha_{sn}Z_{sn}\delta(s-s')\delta(n-n') - \sum_{u=0}^{U}\sum_{w=0}^{W}\sum_{m=0}^{M} \frac{j\omega C_{uwm}\gamma_{s'n'}^{uw}}{M_{uwm}(\omega^2 + 2j\xi_{uwm}\omega_{uwm}\omega - \omega_{uwm}^2)}\gamma_{sn}^{uw}\,. \tag{18}$$

Finally, the modal amplitude vector $\mathbf{B}$ can be solved by Eq. (17).

Substituting Eq. (9) into Eq. (7) yields the following expression of the total sound pressure on the incident side ($z = -D$),

$$P(x,y) = P_i + P_r = \sum_{u=0}^{U}\sum_{w=0}^{W} \frac{Z_{uw}^r A_{uw}}{\beta^{uw}} j\omega\mathbf{B}^T\boldsymbol{\gamma}^{uw}\varphi_{uw}(x,y) + P_{rigid} = \mathbf{G}_1\boldsymbol{\Psi} + F_c\mathbf{G}_2\boldsymbol{\Psi} + P_{rigid}\,, \tag{19}$$

where $\boldsymbol{\gamma}^{uw} = [\gamma_{11}^{uw},...\gamma_{sn}^{uw},...\gamma_{SN}^{uw}]^T$. According to Ref [35], P_{rigid} can be viewed as the surface sound pressure of the MPPA with rigid backing wall under plane wave excitation, $P_{rigid} = \frac{abB_{00}^1 Z_{00}^r}{\beta^{00}} + \frac{jp_0 k_0 ab\mathrm{e}^{\mathrm{j}k_0 D}}{\mu^{00}\beta^{00}} + p_0\mathrm{e}^{\mathrm{j}k_0 D}$. The row vector $\mathbf{G}_1$ and $\mathbf{G}_2$, and the column vector $\boldsymbol{\Psi}$ can be referenced in Appendix A.

According to Eq. (6) and Eq. (9), the surface velocity $v_1(x,y)$ of the SAC-AMPPA can be obtained as,

$$v_1(x,y)=\frac{\partial(\Phi_i+\Phi_r)}{\partial z}|_{z=-D}=\sum_{u=0}^{U}\sum_{w=0}^{W}\frac{A_{uw}}{\beta^{uw}}\,j\omega\mathbf{B}^T\boldsymbol{\gamma}^{uw}\varphi_{uw}(x,y)+v_1^{rigid}=\mathbf{H}_1\boldsymbol{\Psi}+F_c\mathbf{H}_2\boldsymbol{\Psi}+v_1^{rigid}\,. \tag{20}$$

v_1^{rigid} in Eq. (20) is the surface velocity of the MPPA with rigid backing wall under plane wave excitation, $v_1^{rigid}=abB_{00}^1/\beta^{00}$. The row vector $\mathbf{H}_1$ and $\mathbf{H}_2$ can be referenced in Appendix A.

Based on Eqs. (19) and (20), the absorbed sound power of the SAC-AMPPA can be expressed as,

$$\Pi_{abs}=\frac{1}{2}\mathrm{Re}[\int_0^a\int_0^b P(x,y)v_1(x,y)^H\,\mathrm{d}x\mathrm{d}y], \tag{21}$$

where the superscript H denotes complex conjugate. Then, the sound absorption coefficient of the SAC-AMPPA can be obtained by,

$$\alpha=\frac{\Pi_{abs}}{\Pi_{inc}}, \tag{22}$$

where Π_{inc} is the sound power of the incident plane wave, $\Pi_{inc}=|p_0|^2\,ab/2\rho_0c_0$.

2.2. Optimization of the point force

The Eqs. (19) and (20) still contain the unknown variable of the amplitude F_c of the point force. The sound absorption coefficient of the SAC-AMPPA will be maximal when the absorbed sound power in controlled condition reaches the maximum. Hence, Π_{abs} is chosen as the theoretical objective function, by maximizing which the optimal amplitude of the point force can be obtained. Substituting Eq. (19) and Eq. (20) into Eq. (21), the absorbed sound power Π_{abs} can be further expressed as,

$$\Pi_{abs}=\frac{1}{2}\mathrm{Re}[a_1F_cF_c^H]+\frac{1}{2}\mathrm{Re}[b_1F_c]+\frac{1}{2}\mathrm{Re}[c_1F_c^H]+\frac{1}{2}\mathrm{Re}[d_1], \tag{23}$$

where the variables a_1, b_1, c_1 and d_1 can be referenced in Appendix A. The absorbed sound power Π_{abs} is a quadratic function of the amplitude of the point force F_c. Defining F_c as the complex value $F_c(\omega)=F_{c,R}(\omega)+jF_{c,I}(\omega)$, Eq. (23) can be re-expressed as the bivariate quadratic function of the variables $F_{c,R}(\omega)$ and $F_{c,I}(\omega)$,

$$\Pi_{abs} = \frac{1}{2}\mathrm{Re}[a_1]F_{c,R}(\omega)^2 + \frac{1}{2}\mathrm{Re}[a_1]F_{c,I}(\omega)^2 + \frac{1}{2}\mathrm{Re}[b_1 + c_1]F_{c,R}(\omega)$$

$$+\frac{1}{2}\mathrm{Re}[\,j(b_1 - c_1)]F_{c,I}(\omega) + \frac{1}{2}\mathrm{Re}[d_1]. \qquad (24)$$

Deriving the partial derivative of the two real variables $F_{c,R}(\omega)$ and $F_{c,I}(\omega)$, and letting the partial derivative equal zero yields the optimal amplitude of the point force for maximizing the absorbed sound power Π_{abs},

$$F_{c,R}^{opt}(\omega) = -\frac{\mathrm{Re}[b_1 + c_1]}{2\,\mathrm{Re}[a_1]}, F_{c,I}^{opt}(\omega) = -\frac{\mathrm{Re}[\,j(b_1 - c_1)]}{2\,\mathrm{Re}[a_1]}. \qquad (25)$$

Then, the maximum sound absorption coefficient in controlled condition can be obtained.

3. Performance of the SAC-AMPPA

3.1. Parameter assignment and model validation

The geometric and material parameters of the model used in the simulation are listed in Table 1. The dimension of the SAC-AMPPA and the thickness of the backing panel are assigned with different values to verify the control effect. The point force is also located at different positions to explore its impact on the sound absorption improvement. After a careful convergence study, the upper limit numbers of the cavity and panel mode are chosen as $U = W = M = 9$, $S = N = 20$. The increment of the response without control (such as the sound pressure at any position of the cavity) on the upper limit frequency 1000Hz is less than 1dB when the modal numbers further increase, which guarantees the accuracy of the results.

Table 1 The geometric and material parameters of the model

MPP		**Backing panel**	
Parameter	**Value**	**Parameter**	**Value**
Pore diameter of the MPP	0.4×10^{-3} m	The material of the backing panel	Aluminum
Thickness of the MPP	0.5×10^{-3} m	Density of aluminum	2790Kg/m^3
Porosity of the MPP	1%	Young's modulus of aluminum	7.2×10^{10} N/m^2
Cavity depth of the SAC-AMPPA	0.05m	Poisson's ratio of aluminum	0.34
Viscosity coefficient of air	1.882×10^{-5} Pa·s	Modal damping ratio of aluminum	0.005

Density and sound speed of air	$\rho_0 = 1.21\,\mathrm{Kg/m^3}$ $c_0 = 344\,\mathrm{m/s}$	The amplitude of the incident plane wave	p_0=1Pa

In order to validate the theoretical model, the SAC-AMPPA without control is also modeled by the finite element software COMSOL. The length and width of the SAC-AMPPA is set as 0.15m by 0.15m, and the thickness of the backing panel is 0.00052m. The MPP is modeled by the equivalent impedance surface built in COMSOL. The sound absorption coefficients obtained by analytical and numerical methods are shown in Fig.2, in which the sound absorption coefficient of the MPPA with rigid backing wall (traditional MPPA) is also included. General good agreement is found among them, which validates the accuracy of the theoretical model. Compared with the result of the traditional MPPA, two absorption peaks in the low frequency range are seen for the SAC-AMPPA. These two peaks are induced by the resonant vibration of the (1,1) and (1,3) mode of the backing panel, which substantially absorbs and dissipates the incident sound energy [27].

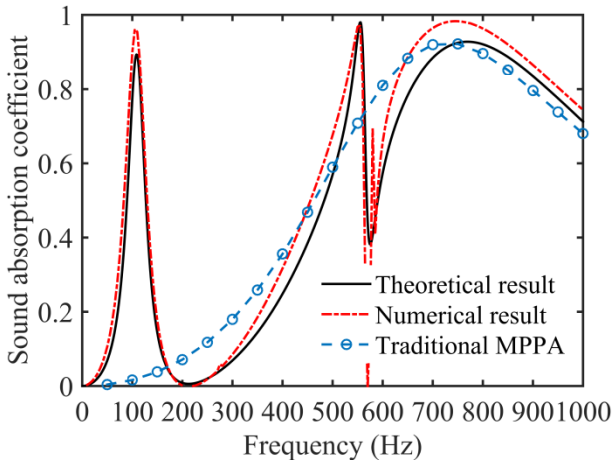

Fig.2. Comparison of the theoretical and numerical results.

3.2. Performance analysis of the SAC-AMPPA

The dimension of the SAC-AMPPA and the thickness of the backing panel are assembled as the following six cases to validate the control performance, which are listed in Table 2. The position of the point force is mainly arranged at four types of locations, i.e., at the corner of the backing panel [P-Case 1, $(0.1a, 0.1b)$], at the middle-line $y = b/2$ except for the center point [P-Case 2, $(0.1a, b/2)$], at the middle-line $x = a/2$ except for the center point [P-Case 3, $(a/2, 0.1b)$], and at the center of the backing panel [P-Case 4, $(a/2, b/2)$].

Table 2 Six cases of parameter combination (the size of the SAC-AMPPA and the backing

panel thickness)

D-Case	Dimension Length×Width	Thickness
D-Case 1 (Experiment)	0.15m×0.15m	0.0004m
D-Case 2 (Theory and experiment)	0.15m×0.15m	0.00052m
D-Case 3 (Experiment)	0.15m×0.15m	0.00072m
D-Case 4 (Theory)	0.3m×0.4m	0.001m
D-Case 5 (Theory)	0.6m×0.8m	0.006m
D-Case 6 (Theory)	0.6m×0.8m	0.003m

The control results for the D-Case 2 and D-Case 4 are shown in Fig.3 and for the D-Case 5 and D-Case 6 are shown in Fig.4. Results obtained demonstrate that the sound absorption is highly improved and achieves perfect sound absorption (absorption coefficient is close to 1) with control in a wide controllable low frequency range, which validates the feasibility of the SAC-AMPPA. The hole-cavity resonant frequency of the MPPA (HC resonance) for the MPP parameter and cavity depth used is 730Hz. The HC resonant frequency of the SAC-AMPPA will change slightly for different cases due to the cavity/panel coupling effect. Hence, its sound absorption performance without control below HC resonant frequency is basically the same for different D-Cases. In general, the controllable bandwidth is correlated with the size of the SAC-AMPPA and the position of the point force. The small sized SAC-AMPPA is beneficial to obtain a very wide controllable bandwidth, such as the D-Case 2 and D-Case 4, in which cases the absorption coefficient can raise to 1 with control in the entire low frequency range below 743 Hz (HC resonance). The controllable bandwidth gradually becomes shorter when the size of the SAC-AMPPA increases, such as the D-Case 5 and D-Case 6. The upper limit controllable frequency is only to 430Hz for these two large sized cases when the point force is located at the optimal position of the center of the backing panel.

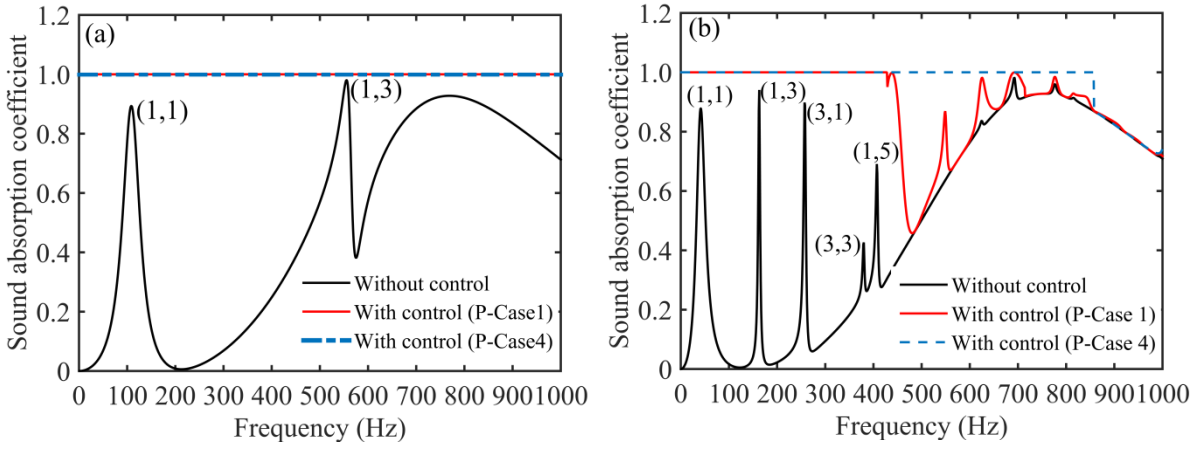

Fig.3. Sound absorption coefficient of the SAC-AMPPA with and without control: (a) D-Case 2, (b) D-

Case 4.

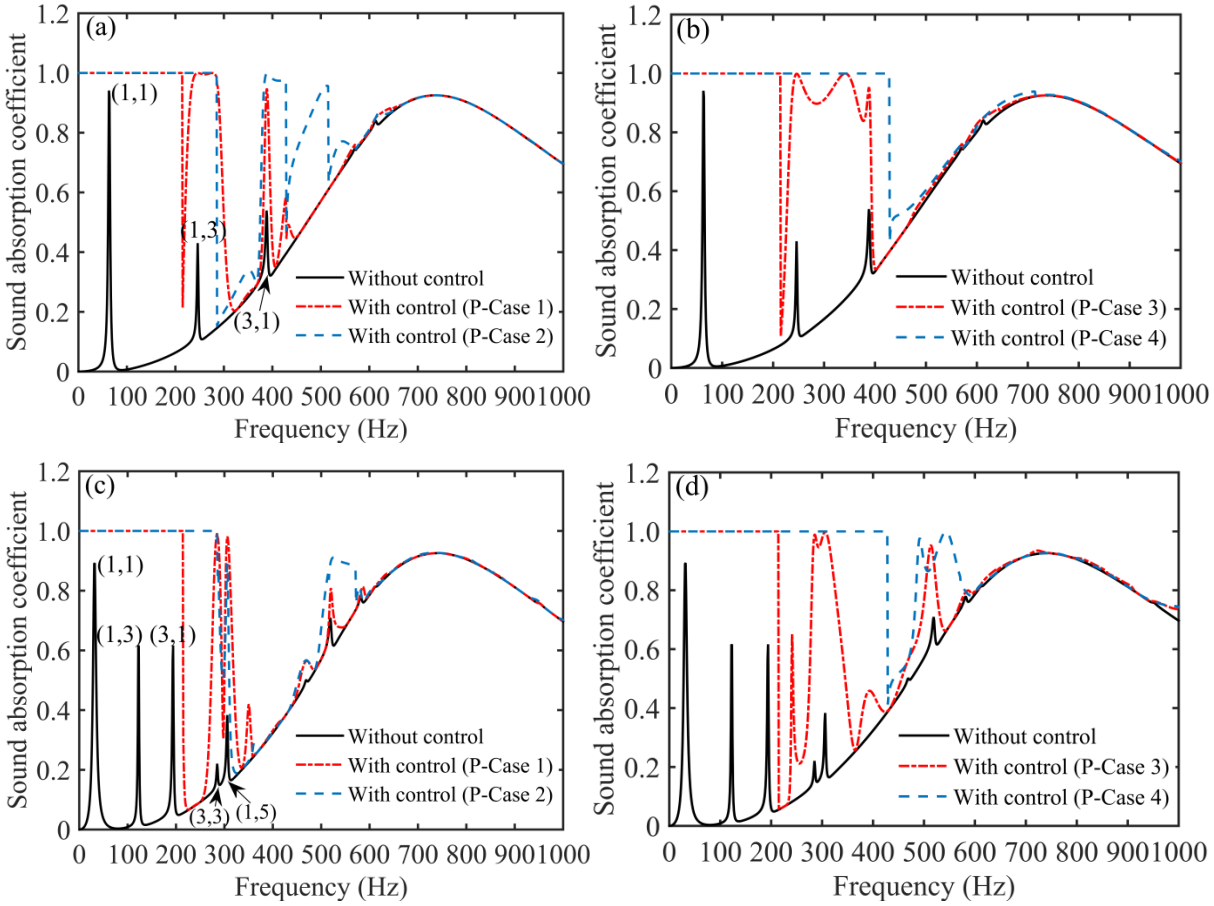

Fig.4. Sound absorption coefficient of the SAC-AMPPA with and without control for the D-Case 5 and D-Case 6: (a) and (b) D-Case 5, (c) and (d) D-Case 6.

The position of the point force is also the key factor affecting the controllable bandwidth of the SAC-AMPPA. Similar to that of the Ref [35], there is an upper limit frequency (cutoff frequency) for each type of the location of the point force, after which the control effect is significantly weakened. The difference is that there are also narrow frequency-bands or a few frequency points above the cutoff frequency in which the sound absorption improvement is remarkable for the SAC-AMPPA. The optimal position is the center of the backing panel (P-Case 4), in which case the controllable bandwidth is the longest and the upper limit controllable frequency is the resonant frequency of the (0,2,0) cavity mode, as shown in Fig.4. The controllable bandwidth is the shortest for the point force being located at the corner of the backing panel (P-Case 1), where the cutoff frequency is only to the resonant frequency of the (0,1,0) cavity mode. Although the cutoff frequency of the P-Case 2 (the resonant frequency of the (1,0,0) mode) is larger than that of the P-Case3 (the resonant frequency of the (0,1,0) mode), the control effect for these two cases is similar due to the fact that there are also controllable narrow frequency-bands above their cutoff frequencies, as shown in Fig.4 (a) and (b). The cutoff

frequency of each type of the point force location for the small sized SAC-AMPPA is higher than that of the large sized case, and the minimum cut-off frequency for the P-Case 1 could be close to the HC resonant frequency of the SAC-AMPPA. Hence, the point force location is not very critical for improving the low frequency sound absorption for the small sized SAC-AMPPA, as shown in Fig.3, where only the optimal and worst locations (P-Case 4 and P-Case 1) are considered. The resonant frequencies of the cavity modes for the D-Case 2, D-Case 4 and D-Case 5 are listed in Table 3 for aiding the analysis. Besides, it can be found from the Fig.4 that the structural parameter of the backing panel has no impact on the control effect below the cutoff frequency of each type of the point force location, which indicates that the modal characteristic of the backing panel (number of the modes and their resonant frequencies) is not the key factor affecting the sound absorption performance in the controllable frequency range. It has a certain impact on the control effect above the cutoff frequency, and the backing panel with low modal density is beneficial for obtaining additional controllable frequency-bands in the P-Case 2 and P-Case3, as shown in Fig.4 (a) and (b).

Table 3 Resonant frequency of the cavity mode for the D-Case 2, D-Case 4 and D-Case 5

Cavity mode	**Resonant frequency (Hz)**		
	D-Case 2	**D-Case 4**	**D-Case 5**
(0,0,0)	0	0	0
(0,1,0)	1147	430	215
(1,0,0)	1147	573	287
(1,1,0)	1622	717	358
(0,2,0)	2293	860	430
(1,2,0)		1034	517
(2,0,0)		1147	573
(0,4,0)			860

4. Experimental validation

4.1. Experimental setup

Experimental tests are carried out to validate the theoretical model of the SAC-AMPPA. The experimental schematic diagram and setup are shown in Fig.5 and Fig.6. The SAC-AMPPA is installed at the left end of the rectangular duct, and the primary sound source (Loudspeaker) is placed at the right end. The cross-section size of the rectangular duct is 0.15m×0.15m, which guarantees the plane wave sound field in the duct below the cutoff frequency (1146Hz) of the duct. The cavity depth of the SAC-AMPPA is about 0.05m. The material of the MPP is steel and the backing panel is aluminum. The thickness of the MPP is 0.5×10^{-3}m, and the thickness of the backing panel is 0.0004m (D-Case 1), 0.00052m (D-Case 2), and 0.00072m (D-Case 3),

respectively. The porosity and perforation diameter of the MPP is 0.5% and 0.5×10^{-3}m. The size of these two plates is 0.175m×0.175m (slightly larger than the sectional size of the duct). They are squeezed by the flanges with rubber ring to simulate the simply supported boundary condition. A small control shaker (Type JZ-2A) is used as the point force, which is located at the optimal position of the P-Case 4. The sound absorption coefficient of the SAC-AMPPA is measured by transfer function method with two microphones and B&K 3050 acquisition front end. The distance between the two microphones is 0.2m, and the distance between the microphone P2 and the MPP is 0.175m, which guarantees that the absorption coefficient measured in frequency range of 50～500Hz is accurate. The amplitude of the incident plane wave is about 0.2Pa～1Pa, which does not affect the measurement of sound absorption coefficient because it is the ratio of the absorbed sound energy to the incident sound energy.

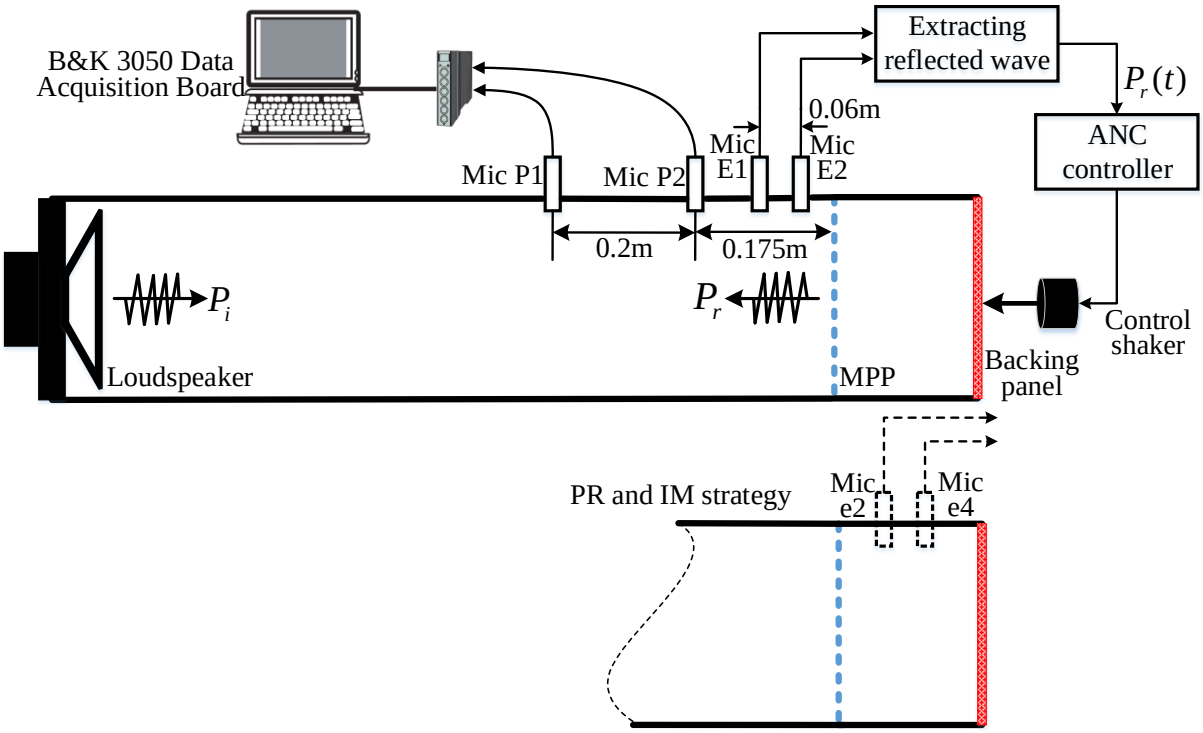

Fig.5. The experimental schematic diagram.

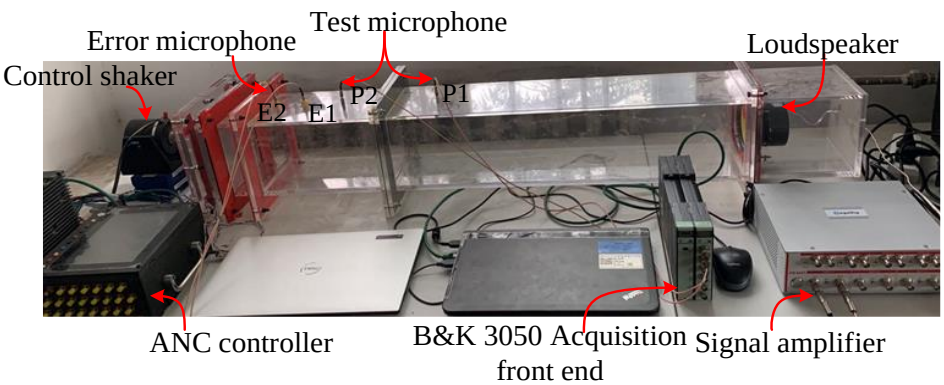

Fig.6. The experimental setup

The sound absorption coefficient is not suitable to be used as the cost function (error signal) for the actual control system because it is not a time-varying signal. Constructing measurable error signal that is highly correlated with the sound absorption coefficient is a key problem for the practical application. Such topic of error sensing strategy will be investigated for the small sized SAC-AMPPA in Section 6. Since the sound field in the duct is the superposition of the incident and reflected plane waves, the reflected plane wave will be minimum when the sound absorption coefficient of the SAC-AMPPA is maximum. Hence, the reflected plane wave can be directly used as the error signal. The reflected plane wave in the duct can be extracted by using two closely arranged microphones (Mic E1 and Mic E2, the spacing is $d = 0.06\text{m}$). The sound pressure $p_e(t)$ and particle velocity $v_e(t)$ on the midpoint of these two microphones are $p_e(t)=(p_{e,1}+p_{e,2})/2$, $v_e(t)=-(1/\rho_0 d)\int_0^t (p_{e,1}-p_{e,2})\mathrm{d}\tau$. Then, the incident and reflected plane wave at this point can be expressed as,

$$p_i(t)=\frac{1}{2}[p_e(t)+\rho_0 c_0 v_e(t)],\ p_r(t)=\frac{1}{2}[p_e(t)-\rho_0 c_0 v_e(t)]. \tag{26}$$

The reflected wave signal is input to the ANC controller (developed by our research group) to iteratively calculate the control signal by using the feed-forward Fx-LMS algorithm. The primary excitation signal is directly used as the reference signal. The amplified control signal is input to the small shaker, which controls the vibration of the backing panel so as to minimize the reflected plane wave. The secondary path is from the shaker drive signal to the reflected wave signal, whose transfer function is measured by off-line modeling method. The sound pressure on the point Mic P1 and Mic P2 is recorded for 5 seconds to calculate the sound absorption coefficient with and without control. The sound absorption coefficients of the empty tube with rigid and open ends are provided in Fig. B, which can validate the effectiveness of the test results. The complex amplitude of the sound pressure at P1 and P2 with control is also provided in Table C.

4.2. Results analysis

The sound absorption coefficient is measured from 50 Hz to 500 Hz with an interval of 10 Hz. The theoretical and experimental results for these three cases are shown in Fig.7-Fig.9. The size of the MPP and backing panel is slightly larger than the theoretical value. The four sides of the backing panel may not be well compressed by the flange, which cannot well simulate the simply supported boundary condition. All these reasons may lead to the resonant frequencies of the backing panel being slightly shifted to the low frequency. Thin plate is more affected by

these interference factors, for instance, especially the 2nd resonant frequency for the D-Case 1. Besides, due to the measurement error, the sound leakage at the edge of the MPP and the difference between experimental system and theoretical model, the measured value of the sound absorption coefficient without control is slightly higher than the theoretical value in the frequency range of 150-350Hz.

Similar as that of the theoretical results, the sound absorption coefficient of the SAC-AMPPA is highly improved with control in experiments. The trends of the sound absorption coefficient both in controlled and uncontrolled conditions in experiments are in good agreement with these of the theoretical results, which qualitatively verifies the theoretical modeling. Besides, the two flanges which are used for squeezing the elastic backing panel are fastened by only eight bolts. The stress on the four sides of the elastic plate may not be uniform, which results that the modal shape of the backing panel for some resonant modes may be slightly distorted. This has a greater impact especially on the thin plates for the D-Case 1, which may be the reason that the sound absorption coefficient is a little undulant with control in the frequency range of 100-250Hz in experiment. On the contrary, the sound absorption coefficient curves with control are smoother for the D-Case 2 and D-Case 3. Besides, the sound absorption coefficient with control is not close to 1 in experiments in the extreme low frequency range below 100Hz. The reason of this is that the point force with large amplitude is needed to excite the backing panel for adjusting the cavity sound field due to the large stiffness of the backing panel in the extreme low frequency range. However, the small control shaker cannot provide enough output force, which results in the limited increment of the sound absorption coefficient.

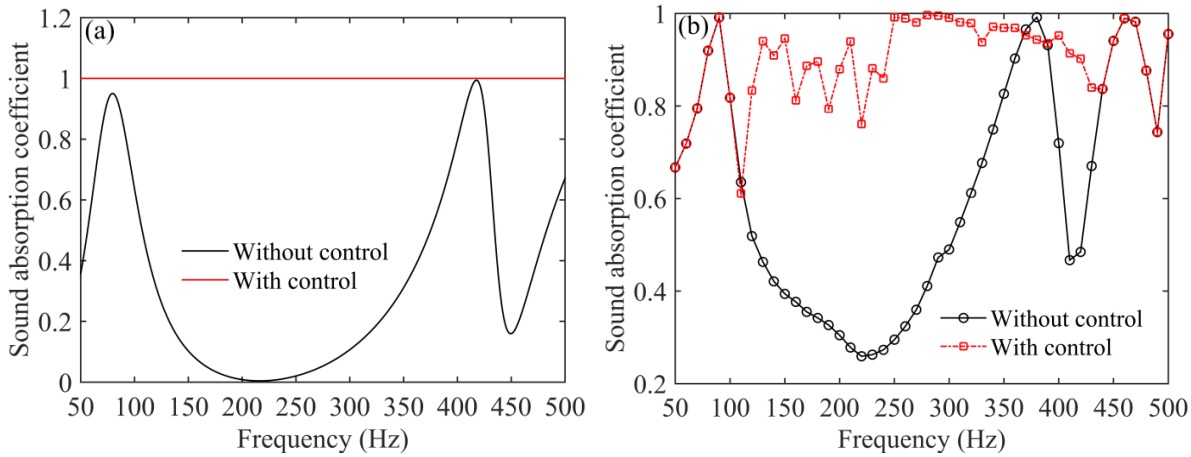

Fig.7. The theoretical and experimental results for the D-Case 1: (a) theory, (b) experiment.

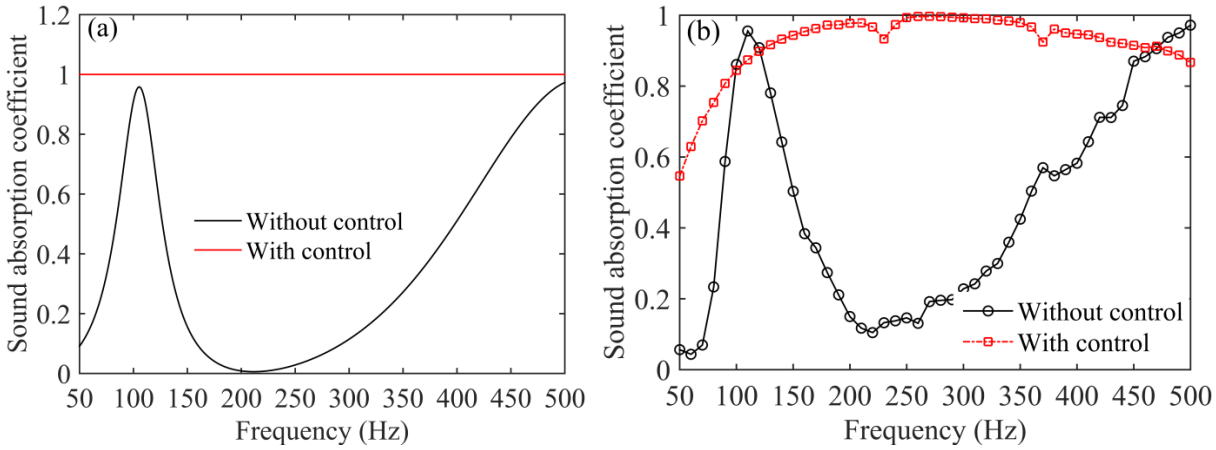

Fig.8. The theoretical and experimental results for the D-Case 2: (a) theory, (b) experiment.

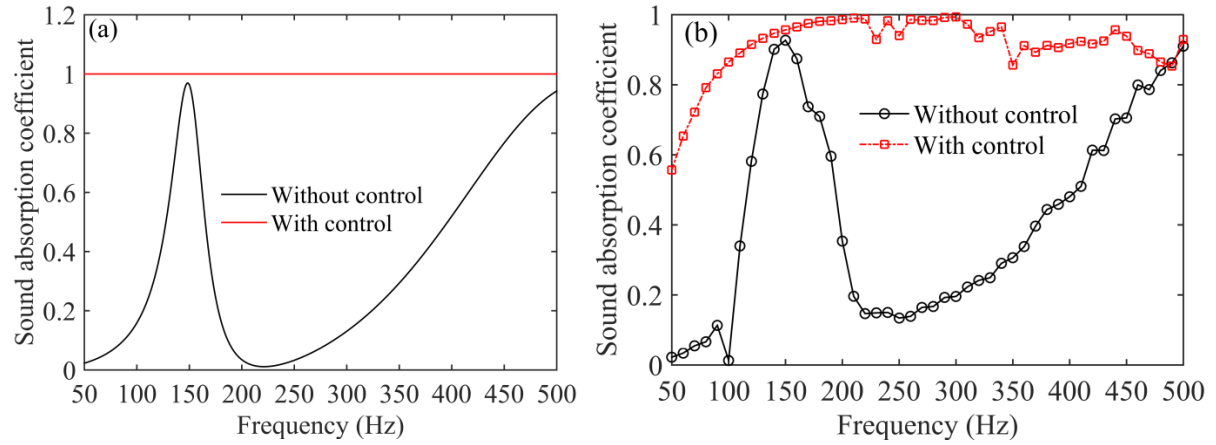

Fig.9. The theoretical and experimental results for the D-Case 3: (a) theory, (b) experiment.

5. Physical mechanism of the sound absorption improvement

Except for the (odd, odd) modes, all other type of the mode of the backing panel can be excited with control. All types of the cavity mode will be also excited due to their coupling effect with the panel mode, which accordingly adjusts the surface sound impedance. Similar as that of the MPPA with irregular-shaped cavity [12], the surface sound impedance exhibits obvious local characteristics due to the varying sound pressure and velocity distribution over the surface of the SAC-AMPPA with control. The surface average impedance is effectively adjusted to close to the characteristic impedance of the air in the controllable frequency-bands under the control of optimal point force, which is the intuitive mechanism of sound absorption improvement. However, the physical nature of the active control and deep-seated reasons of the sound absorption improvement is still unclear. Besides, the difference of contribution of different type of the cavity mode to sound absorption improvement and the reason why there is a controllable upper limit cutoff frequency for each type of the point force location are also still unknown. These will be further explored in the following by analyzing the contribution of the

cavity modes to the sound absorption improvement.

5.1. Absorption mechanism on the resonant frequency of the backing panel without control

In order to clarify the control mechanism in the controllable frequency band, the cause of formation of the sound absorption peak on the resonant frequency of the (odd, odd) mode of the backing panel without control should be firstly explored. The (0,0,0) cavity mode is mainly excited by the incident plan wave in low frequency range. Since the mode pair (cavity/ panel) that has the opposite parity of mode index can couple with each other, the (odd, odd) mode of the backing panel can be resonantly excited, which substantially absorbs the incident sound energy and forms the absorption peaks. Further the (1,3) mode of the backing panel is taken as an example in D-Case 4 (resonant frequency $f=163\text{Hz}$) for aiding the thorough absorption mechanism analysis. It can be found from calculating the amplitudes of the cavity modes that the (0,0,0) and (0,2,0) modes are primarily excited with relative large amplitudes on this resonant frequency. Then, the surface sound pressure $P(x,y)$ and velocity $v_1(x,y)$ of the SAC-AMPPA can be simplified as,

$$P(x,y)=\frac{Z_{00}^{r}A_{00}}{\beta^{00}}\,j\omega\mathbf{B}^{T}\boldsymbol{\gamma}^{00}\varphi_{00}(x,y)+\frac{Z_{02}^{r}A_{02}}{\beta^{02}}\,j\omega\mathbf{B}^{T}\boldsymbol{\gamma}^{02}\varphi_{02}(x,y)+P_{rigid}\,, \tag{27}$$

$$v_1(x,y)=\frac{A_{00}}{\beta^{00}}\,j\omega\mathbf{B}^{T}\boldsymbol{\gamma}^{00}\varphi_{00}(x,y)+\frac{A_{02}}{\beta^{02}}\,j\omega\mathbf{B}^{T}\boldsymbol{\gamma}^{02}\varphi_{02}(x,y)+v_1^{rigid}\,. \tag{28}$$

In Eqs. (27) and (28), the variable $v_1^{rigid}=5.9\times10^{-5}+\text{j}7.4\times10^{-4}(\text{m/s})$ and $P_{rigid}=1.95-\text{j}0.008(\text{Pa})$. v_1^{rigid} is very small and close to 0 and P_{rigid} is close to 2Pa, which indicates that the surface impedance of the MPPA with rigid backing wall has small sound resistance and very large sound reactance on this resonant frequency and its sound absorption is extremely weak. The (0,0,0) cavity mode is firstly excited by the incident plane wave, which further resonantly excites the (1,3) mode of the backing panel (its amplitude is the largest in $\mathbf{B}$). Conversely, the (0,0,0) cavity mode will be further excited by the (1,3) mode due to their coupling effect. The (0,2,0) mode is excited only by the (1,3) mode due to their coupling effect. Accordingly, the surface sound pressure $P(x,y)$ in Eq. (27) can be viewed as the superposition of three components, i.e., the sound pressure P_{rigid}, the sound pressure contributed by the (1,3) mode excited-(0,0,0) cavity mode $P^{00}=\frac{Z_{00}^{r}A_{00}}{\beta^{00}}\,j\omega\mathbf{B}^{T}\boldsymbol{\gamma}^{00}\varphi_{00}(x,y)$, and the sound pressure

contributed by the (1,3) mode excited-(0,2,0) cavity mode $P^{02} = \frac{Z_{02}^r A_{02}}{\beta^{02}} j\omega \mathbf{B}^T \boldsymbol{\gamma}^{02} \varphi_{02}(x,y)$. Similarly, the surface velocity $v_1(x,y)$ in Eq. (28) can also be roughly viewed as the superposition of two components when v_1^{rigid} is ignored, i.e., the velocity contributed by the (1,3) mode excited-(0,0,0) mode (denoted by v_1^{00}), and the velocity contributed by the (1,3) mode excited-(0,2,0) mode (denoted by v_1^{02}).

By neglecting v_1^{rigid}, the absorbed sound power of the SAC-AMPPA on this resonant frequency can be expressed as,

$$\Pi_{abs}^{(1,3)} = \frac{1}{2}\int_0^a \int_0^b \mathrm{Re}[P(x,y) v_1(x,y)^H] \mathrm{d}x\mathrm{d}y$$

$$= \frac{1}{2}\mathrm{Re}[Z_{00}^r \left| \frac{A_{00}}{\beta^{00}} j\omega \mathbf{B}^T \boldsymbol{\gamma}^{00} \right|^2 \beta^{00}] + \frac{1}{2}\mathrm{Re}[\frac{Z_{00}^r A_{00}}{\beta^{00}} j\omega \mathbf{B}^T \boldsymbol{\gamma}^{00} (\frac{A_{02}}{\beta^{02}} j\omega \mathbf{B}^T \boldsymbol{\gamma}^{02})^H \int_0^a \int_0^b \varphi_{00}\varphi_{02} \mathrm{d}x\mathrm{d}y]$$

$$+ \frac{1}{2}\mathrm{Re}[\frac{Z_{02}^r A_{02}}{\beta^{02}} j\omega \mathbf{B}^T \boldsymbol{\gamma}^{02} (\frac{A_{00}}{\beta^{00}} j\omega \mathbf{B}^T \boldsymbol{\gamma}^{00})^H \int_0^a \int_0^b \varphi_{00}\varphi_{02} \mathrm{d}x\mathrm{d}y] + \frac{1}{2}\mathrm{Re}[Z_{02}^r \left| \frac{A_{02}}{\beta^{02}} j\omega \mathbf{B}^T \boldsymbol{\gamma}^{02} \right|^2 \beta^{02}]$$

$$+ \frac{1}{2}\mathrm{Re}[(\frac{A_{00}}{\beta^{00}} j\omega \mathbf{B}^T \boldsymbol{\gamma}^{00})^H P_{rigid} \int_0^a \int_0^b \varphi_{00} \mathrm{d}x\mathrm{d}y] + \frac{1}{2}\mathrm{Re}[(\frac{A_{02}}{\beta^{02}} j\omega \mathbf{B}^T \boldsymbol{\gamma}^{02})^H P_{rigid} \int_0^a \int_0^b \varphi_{02} \mathrm{d}x\mathrm{d}y]$$

$$= \frac{1}{2}\mathrm{Re}[Z_{00}^r \left| \frac{A_{00}}{\beta^{00}} j\omega \mathbf{B}^T \boldsymbol{\gamma}^{00} \right|^2 \beta^{00}] + \frac{1}{2}\mathrm{Re}[Z_{02}^r \left| \frac{A_{02}}{\beta^{02}} j\omega \mathbf{B}^T \boldsymbol{\gamma}^{02} \right|^2 \beta^{02}] + \frac{1}{2}\mathrm{Re}[(\frac{A_{00}}{\beta^{00}} j\omega \mathbf{B}^T \boldsymbol{\gamma}^{00})^H P_{rigid} ab] \quad .(29)$$

It can be found from Eq. (29) that the absorbed sound power $\Pi_{abs}^{(1,3)}$ also breaks into three types of components, i.e., the self-absorbed sound power of the cavity mode (such as the items 1 and 4, $\Pi(P^{00}, v_1^{00}) = \frac{1}{2}\int_0^a \int_0^b \mathrm{Re}[P^{00}(v_1^{00})^H] \mathrm{d}x\mathrm{d}y$ and $\Pi(P^{02}, v_1^{02})$), the mutual-absorbed sound power between different cavity modes (such as the items 2 and 3, $\Pi(P^{00}, v_1^{02}) = \frac{1}{2}\int_0^a \int_0^b \mathrm{Re}[P^{00}(v_1^{02})^H] \mathrm{d}x\mathrm{d}y$ and $\Pi(P^{02}, v_1^{00})$), and the incremental-absorbed sound power $\Pi(P_{rigid}, v_1^{00})$ and $\Pi(P_{rigid}, v_1^{02})$. Since $Z_{00}^r = \frac{-j\omega\rho_0}{\mu^{00}} = -\rho_0 c_0$, the self-absorbed

sound power of the (0,0,0) mode $\Pi(P^{00}, v_1^{00})$ is negative and equals to -9.0$\times$10^{-5}W, which indicates that it radiates sound energy towards the outside of the SAC-AMPPA and is counterproductive for sound absorption. On account of $Z_{02}^r = \frac{-j\omega\rho_0}{\mu^{02}} = -j\omega\rho_0 \Big/ \sqrt{(\frac{\omega_{02}}{c_0})^2 - (\frac{\omega}{c_0})^2}$ (ω_{02}=$2\pi f_{02}$ is the resonant frequency of the $(0,2)$ section mode, $f_{02} = \frac{c_0}{2}\sqrt{(\frac{0}{a})^2 + (\frac{2}{b})^2}$), Z_{02}^r is imaginary number and the self-absorbed sound power of the (0,2,0) mode $\Pi(P^{02}, v_1^{02})$ is 0 for the low frequency range below its resonant frequency, which indicates that it has no contribution to the sound absorption. The mutual-absorbed sound power $\Pi(P^{00}, v_1^{02})$ and $\Pi(P^{02}, v_1^{00})$, and the incremental-absorbed sound power $\Pi(P_{rigid}, v_1^{02})$ also have no contribution to the sound absorption because of $\int_0^a \int_0^b \varphi_{00}\varphi_{02} \mathrm{d}x\mathrm{d}y = 0$ and $\int_0^a \int_0^b \varphi_{02} \mathrm{d}x\mathrm{d}y = 0$. Hence, the incremental-absorbed sound power $\Pi(P_{rigid}, v_1^{00})$ must be positive (equal to 2.1$\times$10^{-4}W) and the net absorbed sound power of the SAC-AMPPA is $\Pi(P_{rigid}, v_1^{00}) - \Pi(P^{00}, v_1^{00})$ (equal to 1.2$\times$10^{-4}W and close to the incident sound power 1.4$\times$10^{-4}W), which is the main reason for producing the absorption peak on this resonant frequency. The situation for other absorption peaks on these resonant frequencies of the (odd, odd) modes of the backing panel in D-Case 4 is similar. The (0,2,0) cavity mode will be highly excited by the high order (odd, odd) mode, such as the 4th and 5th resonant peaks, but it doesn't contribute to sound absorption on these resonant peaks because the resonant frequencies of these panel modes are lower than that of the (0,2,0) mode. Hence, the sound absorption of the SAC-AMPPA in the low frequency range in D-Case 4 is mainly is dominated by the (0,0,0) cavity mode. The sound absorption coefficient of the SAC-AMPPA in D-Case 4 is also calculated for only considering the (0,0,0) mode in the cavity, as shown in Fig.10 (a). These two results are very consistent, which validates the above analysis. It should be further noticed that v_1^{rigid} cannot be ignored with the increase of frequency, and the incremental-absorbed sound power $\Pi(P^{00}, v_1^{rigid})$ and the absorbed sound power of the MPPA with rigid backing wall $\Pi(P_{rigid}, v_1^{rigid})$ should be considered in Eq. (29).

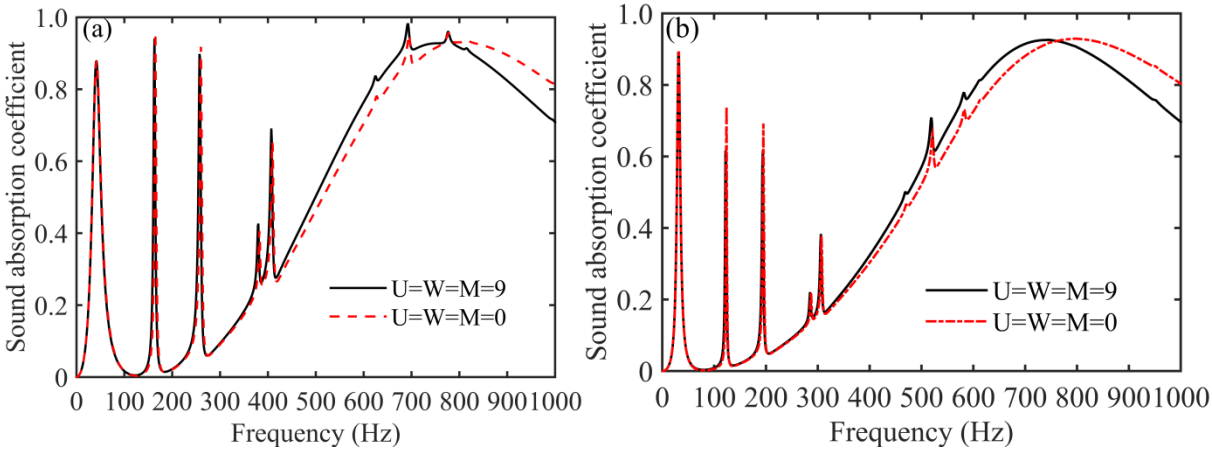

Fig.10. Sound absorption coefficient for these cases of $U=W=M=9$ and $U=W=M=0$: (a) D-Case 4, (b) D-Case 6.

Besides, the amplitude of the sound absorption peaks for the D-Case 5 and D-Case 6 is relatively small, which is due to the lower radiation efficiency of the panel mode for the thick backing panel. The thick panel is used for the large sized SAC-AMPPA for the purpose of reducing the number of panel mode to simplify the analysis. Despite all this, the higher order (odd, odd) modes are also included in the low frequency range below 743Hz for the large sized case. Their radiation efficiency is also low, which makes it difficult to have obvious sound absorption peaks, such as in the frequency band 400Hz-743Hz, as shown in Fig.4. It should be noticed that the self-absorbed sound power of the (0,2,0) mode $\Pi(P^{02}, v_1^{02})$ will be negative and counterproductive to the sound absorption when $f > 430\,\text{Hz}$, which is another reason of not appearing obvious sound absorption peaks in 430Hz-743Hz for the large sized SAC-AMPPA. In short, the (0,0,0) cavity mode also plays the leading role for the sound absorption in the low frequency range for the large sized case, which is validated in Fig.10 (b). Table 4 lists the resonant frequency of the panel mode in D-Case 4, D-Case 5 and D-Case 6 for aiding the analysis.

Table 4 The resonant frequency of the backing panel for D-Case 4, D-Case 5 and D-Case 6

D-Case 4		D-Case 5		D-Case 6	
Modal index	**Resonant frequency (Hz)**	**Modal index**	**Resonant frequency (Hz)**	**Modal index**	**Resonant frequency (Hz)**
(1,1)	43	(1,1)	64	(1,1)	32
(1,2)	88	(1,2)	133	(1,2)	66
(2,1)	124	(2,1)	186	(2,1)	93
(1,3)	165	(1,3)	247	(1,3)	124
(2,2)	170	(2,2)	255	(2,2)	128
(2,3)	247	(2,3)	370	(2,3)	185

(3,1)	260	(3,1)	390	(3,1)	195
(1,4)	272	(1,4)	408	(1,4)	204
(3,2)	306	(3,2)	459	(3,2)	230
(2,4)	353	(2,4)	531	(2,4)	265
(3,3)	383	(3,3)	574	(3,3)	287
(1,5)	410	(1,5)	615	(1,5)	307
(4,1)	451	(4,1)	676	(4,1)	338
(3,4)	490	(3,4)	735	(3,4)	367
(2,5)	492			(2,5)	369
(4,2)	497			(4,2)	373
(4,3)	573			(4,3)	430
(1,6)	578			(1,6)	434
(3,5)	628			(3,5)	471

5.2. Absorption mechanism with control for point force locating at P-Case 4

For further analyzing the control mechanism, the sound absorption performance for the point force being located at P-Case 4 in the D-Case 4 is firstly analyzed thoroughly. The control mechanism for the point force locating at the center of the backing panel (P-Case 4) is nearly the same with the absorption mechanism on the resonant frequency of the (odd, odd) mode without control analyzed in Sec.5.1. Since these (odd, odd) modes are weakly excited with very small amplitudes on the off-resonant frequency without control, the surface sound pressure and velocity of the SAC-AMPPA are close to P_{rigid} and v_1^{rigid} . The sound absorption performance of the SAC-AMPPA is weak, which is similar as that of the MPPA with rigid backing wall. Then, these (odd, odd) modes will also be highly excited on the off-resonant frequency under the control of point force (P-Case 4), which further mainly excites the (0,0,0), (0,2,0) or other (even, even) cavity modes, as shown in Fig.11 in which $f = 200\,\mathrm{Hz}$ is considered. The surface sound pressure $P(x,y)$, the velocity $v_1(x,y)$, and the absorbed sound power Π_{abs} can also be expressed in forms similar to Eq. (27)-Eq. (29). The self-absorbed sound power of the (odd, odd) modes excited-(0,0,0) cavity mode subtracted from the sum of the incremental-absorbed sound power $\Pi(P_{rigid}, v_1^{00})$ and $\Pi(P^{00}, v_1^{rigid})$ is the increased absorbed sound power, which is close to the incident sound power and increases the sound absorption coefficient to 1.

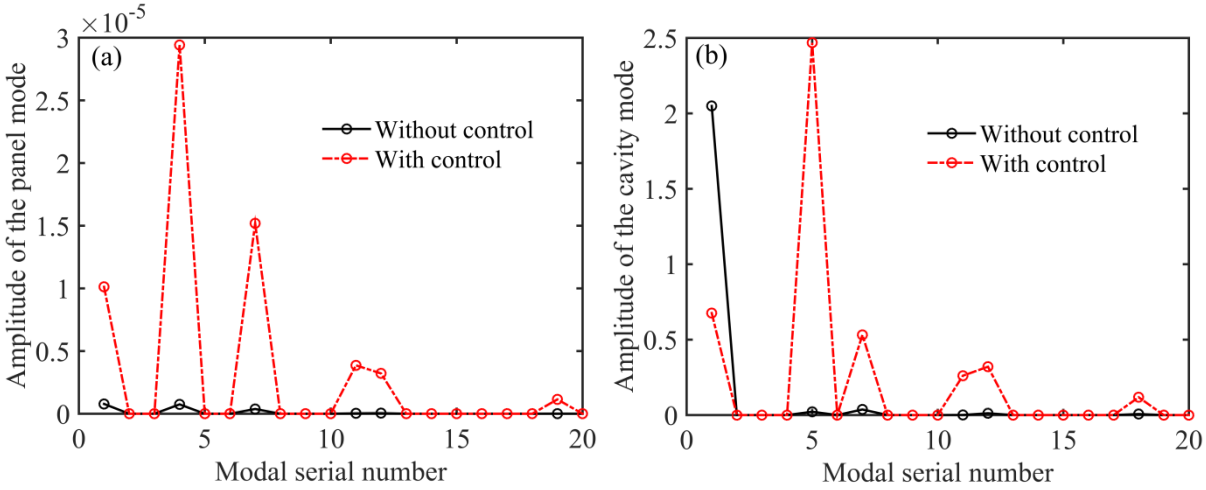

Fig.11. The amplitude of the backing panel and cavity mode: (a) backing panel, (b) cavity.

In general, the surface sound pressure P_{rigid} will be significantly reduced to $P_{rigid} + \frac{Z_{00}^{r} A_{00}}{\beta^{00}} j\omega \mathbf{B}^{T} \boldsymbol{\gamma}^{00} \varphi_{00}(x, y)$ when the incident sound power is absorbed substantially with control. Hence, $\frac{Z_{00}^{r} A_{00}}{\beta^{00}} j\omega \mathbf{B}^{T} \boldsymbol{\gamma}^{00} \varphi_{00}(x, y)$ and P_{rigid} are anti-phase, which indicates that the (odd, odd) modes excited-(0,0,0) cavity mode and the incident plane wave excited-(0,0,0) cavity mode are also anti-phase. This results in the reduced amplitude of this mode with control, as shown in Fig. 11(b). The (0,0,0) cavity mode is also dominant in the control process, which is further validated by the control result of only considering the (0,0,0) mode in Fig. 12 and the surface sound intensity distribution in Fig.13 when $f = 200\,\mathrm{Hz}$. The control result is almost consistent with that of the Fig. 3(b). The surface sound intensity with control can be viewed as the superposition of that of the (0,2) mode and a positive constant quantity (the sound intensity distribution of the (0,2) mode shifting in the positive direction). The average sound intensity of the (0,2) mode is 0, which indicates its zero contribution to sound absorption. The constant quantity is related with the increased absorbed sound power.

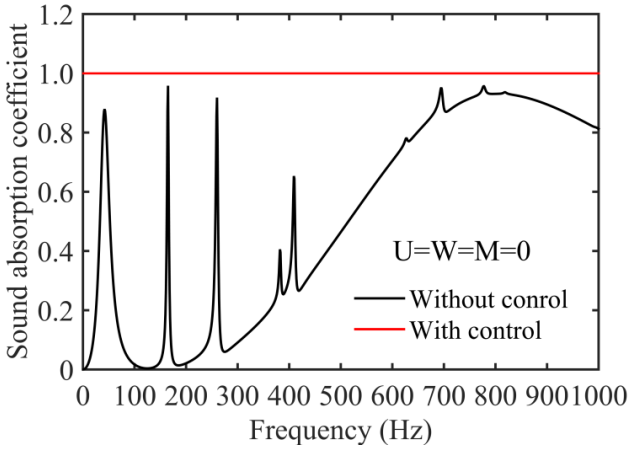

Fig.12. The control result of only considering the (0,0,0) mode.

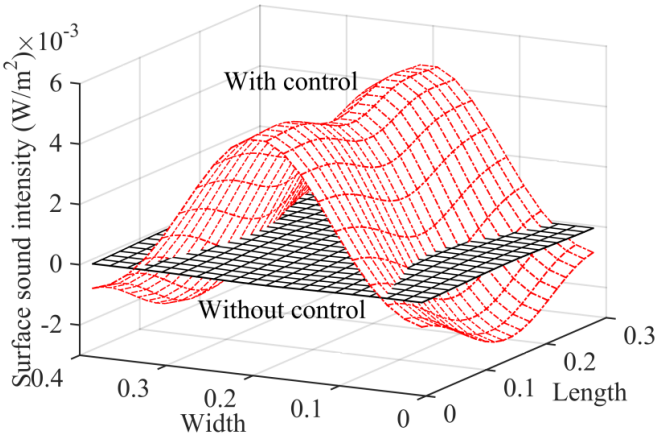

Fig.13. The surface sound intensity distribution with and without control.

5.3. Absorption mechanism with control for point force locating at P-Case 1

All types of the panel modes and cavity modes will be excited by the point force when it is located at the corner of the backing panel (P-Case 1). Without losing generality, the surface sound pressure and velocity of the SAC-AMPPA can be expressed as Eq. (19) and Eq. (20) on each excitation frequency. Then, the absorbed sound power of the SAC-AMPPA with control Π_{abs} in Eq. (23) can be re-expressed as,

$$\Pi_{abs}=\frac{1}{2}\mathrm{Re}[Z_{00}^{r}\left|\frac{A_{00}}{\beta^{00}}j\omega\mathbf{B}^{T}\boldsymbol{\gamma}^{00}\right|^{2}\beta^{00}]+\frac{1}{2}\mathrm{Re}[Z_{01}^{r}\left|\frac{A_{01}}{\beta^{01}}j\omega\mathbf{B}^{T}\boldsymbol{\gamma}^{01}\right|^{2}\beta^{01}]+\cdots+$$

$$\frac{1}{2}\mathrm{Re}[Z_{uw}^{r}\left|\frac{A_{uw}}{\beta^{uw}}j\omega\mathbf{B}^{T}\boldsymbol{\gamma}^{uw}\right|^{2}\beta^{uw}]+\cdots+\frac{1}{2}\mathrm{Re}[Z_{UW}^{r}\left|\frac{A_{UW}}{\beta^{UW}}j\omega\mathbf{B}^{T}\boldsymbol{\gamma}^{UW}\right|^{2}\beta^{UW}]+$$

$$\frac{1}{2}\mathrm{Re}[(\frac{A_{00}}{\beta^{00}}j\omega\mathbf{B}^{T}\boldsymbol{\gamma}^{00})^{H}P_{rigid}ab]+\frac{1}{2}\mathrm{Re}[\frac{Z_{00}^{r}A_{00}}{\beta^{00}}j\omega\mathbf{B}^{T}\boldsymbol{\gamma}^{00}(v_{1}^{rigid})^{H}ab]+\frac{1}{2}\mathrm{Re}[P_{rigid}(v_{1}^{rigid})^{H}ab]$$

$$= \Pi(P^{00}, v_1^{00}) + \Pi(P^{01}, v_1^{01}) + \cdots + \Pi(P^{uw}, v_1^{uw}) + \cdots + \Pi(P^{UW}, v_1^{UW}) + \Pi(P_{rigid}, v_1^{00})$$

$$+\Pi(P^{00}, v_1^{rigid}) + \Pi(P_{rigid}, v_1^{rigid}), \qquad (30)$$

where $Z_{uw}^r = \dfrac{-j\omega\rho_0}{\mu^{uw}} = -j\omega\rho_0 \Big/ \sqrt{(\dfrac{\omega_{uw}}{c_0})^2 - (\dfrac{\omega}{c_0})^2}$. The absorbed sound power is also consists of three components, i.e., the self-absorbed sound power of the panel mode excited-cavity mode $\Pi(P^{uw}, v_1^{uw})$, the incremental-absorbed sound power $\Pi(P_{rigid}, v_1^{00})$ and $\Pi(P^{00}, v_1^{rigid})$, and the absorbed sound power $\Pi(P_{rigid}, v_1^{rigid})$ of the MPPA with rigid backing wall. The mutual-absorbed sound power between different cavity modes $\Pi(P^{uw}, v_1^{u'w'})$ or $\Pi(P^{u'w'}, v_1^{uw})$ is 0 due to $\int_0^a \int_0^b \varphi_{uw}\varphi_{u'w'} \mathrm{d}x\mathrm{d}y = 0$. Since $Z_{00}^r = -\rho_0 c_0$, $\Pi(P^{00}, v_1^{00})$ is always negative. For other $(u, w, 0)$ cavity mode, Z_{uw}^r is imaginary number and the self-absorbed sound power $\Pi(P^{uw}, v_1^{uw})$ is 0 when $\omega < \omega_{uw}$. Z_{uw}^r will be negative real number and the self-absorbed sound power $\Pi(P^{uw}, v_1^{uw})$ will be also negative when $\omega \geq \omega_{uw}$.

Hence, the control mechanism is also similar with that of the point force locating at P-Case 4 when $\omega < \omega_{01}$. Although these high order cavity modes can be excited, they do not contribute to the improvement of sound absorption. Z_{01}^r will be a very large negative number when ω just exceeds ω_{01} . Then, the self-absorbed sound power of the (0,1,0) mode $\Pi(P^{01}, v_1^{01})$ will change from 0 to a very large negative number and has a negative effect on sound absorption, which leads to a sharp decline in control performance. This is the reason that the controllable cutoff frequency of the location of P-Case 1 is the resonant frequency of the (0,1,0) mode, as shown in Fig.3 (b) and Fig. 4 (a) and (c). The self-absorbed power of more cavity modes will be negative with the increase of frequency, which results in the poor control effect in the frequency range above the cutoff frequency. The amplitudes of the panel and cavity modes are shown in Fig. 14 when $f = 200\,\mathrm{Hz}$ for D-Case 4. Although many panel and cavity modes are excited, only these (odd, odd) panel modes excited-(0,0,0) cavity mode plays a key role in the improvement of sound absorption, which offsets the incident plane wave excited-(0,0,0) mode and weakens the amplitude, as shown in Fig.14 (b). The surface sound intensity distribution mainly presents the form of (1,1,0) mode and the net sound intensity is correlated with the

increased absorbed sound power, as shown in Fig.15.

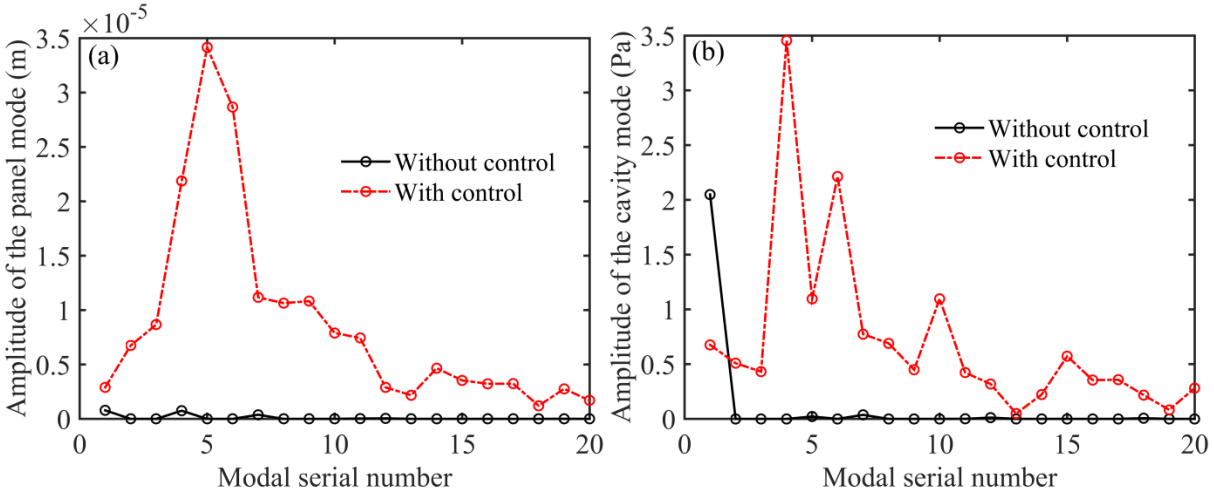

Fig.14. The amplitude of the backing panel and cavity mode: (a) backing panel; (b) cavity.

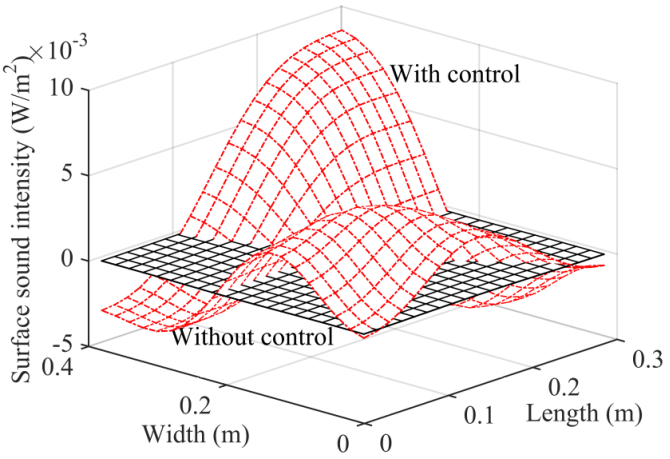

Fig.15. The surface sound intensity distribution with and without control.

Similarly, the self-absorbed sound power of the (0,2,0) mode $\Pi(P^{02}, v_1^{02})$ will be negative when $\omega \geq \omega_{02}$, which results in the resonant frequency of the (0,2,0) mode being the controllable cutoff frequency of the location P-Case 4, as shown in Fig.3 (b) and Fig. 4 (b) and (d). The (s,n) mode with $n = 2,4,...,\text{even}$ of the backing panel cannot be excited when the point force locates at P-Case 2, which results that the (0,1,0) cavity mode cannot be excited. Then, the self-absorbed sound power of the (1,0,0) mode $\Pi(P^{10}, v_1^{10})$ will be negative when $\omega \geq \omega_{10}$, which results the $f_{(1,0,0)}$ being the cutoff frequency of P-Case 2. Although the (1,0,0) cavity mode cannot be excited, but the (0,1,0) mode can still be excited when the point force locates at P-Case 3. Hence, the control performance is significantly reduced and there is a sound

absorption trough when $\omega \geq \omega_{01}$ for P-Case 3, as shown in Fig.4 (c) and (d). Compared with the P-Case 1, there is also a controllable narrowband above the resonant frequency of the (0,1,0) mode because of the self-absorbed sound power $\Pi(P^{10}, v_1^{10}) = 0$. $\Pi(P^{01}, v_1^{01})$ will gradually decrease as the frequency increases, and the net absorbed sound power $\Pi(P_{rigid}, v_1^{00}) + \Pi(P^{00}, v_1^{rigid}) + \Pi(P_{rigid}, v_1^{rigid}) - \Pi(P^{01}, v_1^{01})$ will again reach its maximum in the narrowband around the resonant frequency of the (1,0,0) mode. In short, the optimal location of the point force is P-Case 4, which can gain the widest controllable frequency band and the upper limit cutoff frequency is the resonant frequency of the (0,2,0) mode. The worst location of the point force is P-Case 1, in which case the cutoff frequency can only be up to the resonant frequency of the (0,1,0) mode.

6. Error sensing strategy

Since only the (0,0,0) cavity mode works in the improvement of sound absorption with control, the PR and IM strategies can also be used to simplify the error sensing strategy. The sound field in the cavity will be uniform with control for the small sized SAC-AMPPA when the point force locates at the optimal position of P-Case 4. The (0,2,0) or other high order (even, even, 0) mode will be weakly excited in this case due to their high resonant frequencies, which guarantees the uniform sound field in the cavity with control. Hence, the cavity sound field can be approximately viewed as the superposition of the incident forward plane wave and reflected plane wave, which is conducive to the implementation of PR and IM strategies similar as that in Ref [35]. The cavity sound filed distribution of the SAC-AMPPA with and without control is shown in Fig.16 for the D-Case 2 with P-Case 4 when $f = 60$ Hz and $f = 450$ Hz, in which only the y-z plane ($x = a/2$) is considered. The sound field is nearly uniform with control and slightly affected by the radiated sound field of the backing panel, which validates the above analysis.

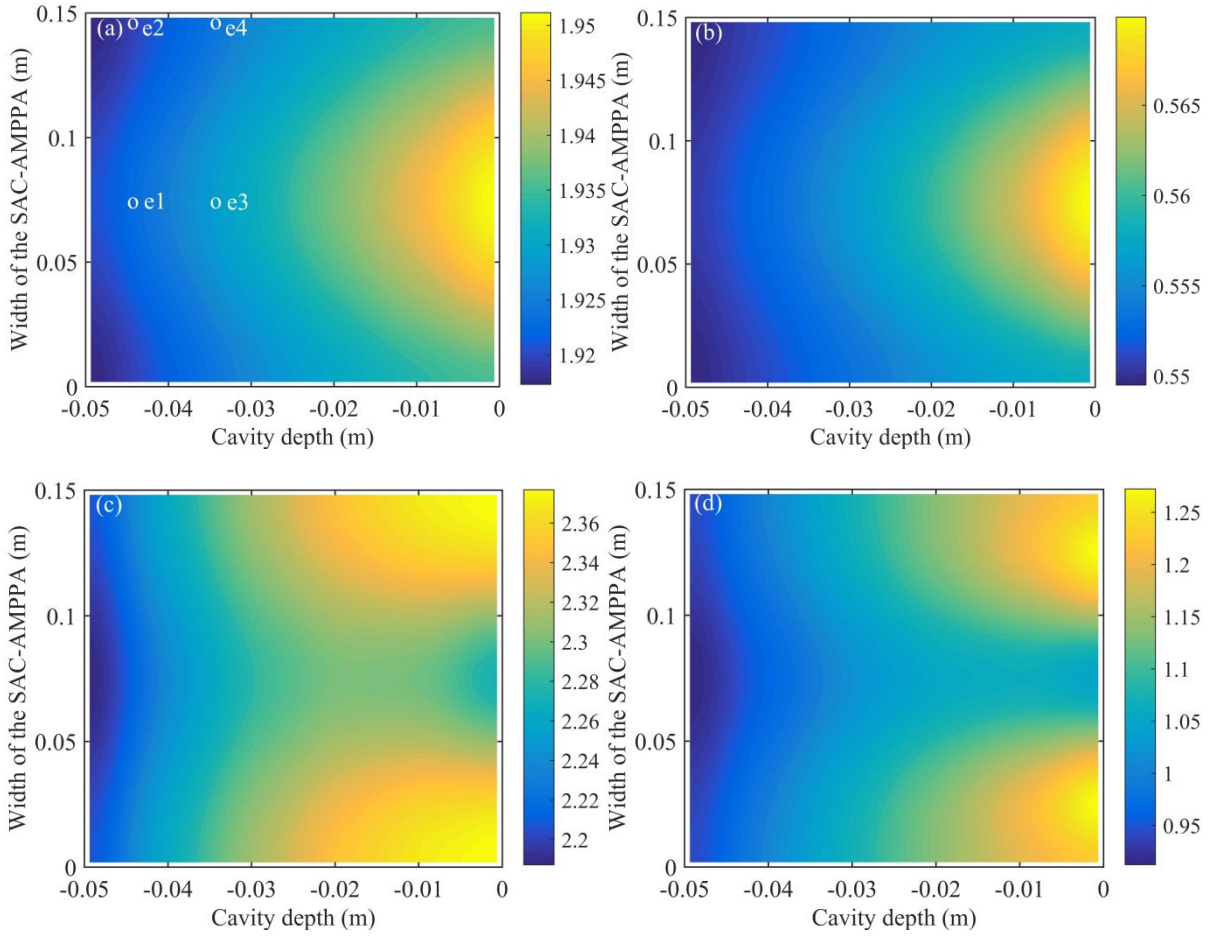

Fig.16. Cavity sound field distribution for D-Case 2: (a) without control ($f=60$ Hz), (b) with control ($f=60$ Hz), (c) without control ($f=450$ Hz), (d) with control ($f=450$ Hz).

It can be considered that the PR strategy of the SAC-AMPPA adjusts the velocity of the backing panel to an appropriate value so that the incident plane wave can be cancelled by the reflected wave in the cavity, which indirectly adjusts the surface impedance close to that of air. Two microphones are needed to sense the sound pressure of the (0,0,0) mode, which are located at the position of e1 (the center of the cavity close to MPP) and e2 (the top of the cavity), as shown in Fig.16 (a). Then, the average sound pressure of these two points $P_{c,1}^{ave}=[P_{c,e1}(x_{e1},y_{e1},z_{e1})+P_{c,e2}(x_{e2},y_{e2},z_{e2})]/2$ can eliminate the sound field component of (0,2,0) mode and represents the sound pressure component of the (0,0,0) mode in the x-y plane passing through the error sensing points e1 and e2 (E1 x-y plane), which can guarantee good control effect in a relative wide low frequency range. Taking $P_{c,1}^{ave}$ as the cost function and letting $P_{c,1}^{ave}=0$, the optimal control force $F_{c,e}^{PR}$ and the optimal control performance of the PR strategy can be obtained.

The IM strategy adjusts the velocity of the backing panel to an appropriate value to absorb most of the reflected plane wave in the cavity, which can indirectly adjust the surface impedance close to that of air. The particle velocity $v_{c,1}^{ave}$ corresponding to $P_{c,1}^{ave}$ can be obtained by the relation $v_{c,1}^{ave} = -(1/j\omega\rho_0)\partial P_{c,1}^{ave}/\partial z$, and then, the sound pressure of the reflected plane wave $P_{c,e}^{r}$ in the cavity can be obtained by Eq. (26). Letting $P_{c,e}^{r} = 0$, the optimal control force $F_{c,e}^{IM}$ and the control performance of the IM strategy can be obtained. Four microphones are needed in practice for accurately extracting the reflected plane wave $P_{c,e}^{r}$. The average sound pressure $P_{c,2}^{ave} = [P_{c,e3}(x_{e3}, y_{e3}, z_{e3}) + P_{c,e4}(x_{e4}, y_{e4}, z_{e4})]/2$ in the x-y plane passing through the error sensing points e3 and e4 (E2 x-y plane) can be measured by the microphones e3 and e4. Then, the reflected plane wave $P_{c,e}^{r}$ can be obtained using the method mentioned in Sec.4.1 with the average sound pressure $P_{c,1}^{ave}$ in E1 x-y plane and $P_{c,2}^{ave}$ in E2 x-y plane.

The control results of these two strategies are shown in Fig.17 (a) for D-Case 2 with P-Case 4, in which the error microphones e1(0.075,0.075,-0.048) and e2(0.075,0.148,-0.048) are used and the MPP parameters are these used in Sec.4. The sound absorption coefficient is highly improved and nearly close to 1 with control in the low frequency range below 500Hz, which validates the feasibility of the PR and IM strategies. The performance of IM strategy is slightly better than PR strategy, which is due to the reasons that the cavity sound field of the SAC-AMPPA is weakened and not completely offset for the optimal control state, as shown in Fig.16. The cavity sound field with control for the IM strategy is closer to that of the optimal control state, which produces better control performance. The performance of the PR and IM strategies is also validated by experimental test. For simplicity, only one error microphone locating at e2 (0.075, 0.145,-0.04) is used to sense the cavity sound field for the PR strategy, which is used as the error signal (cost function) and input to the ANC controller to iteratively calculate the control signal, as shown in Fig.5. Similarly, two microphones locating at e2 (0.075, 0.145,-0.04) and e4 (0.075, 0.145,-0.01) (The spacing is $d = 0.03$m) is used to sense the sound pressure of the reflect plane wave for the IM strategy. The secondary path for the PR strategy is from the shaker drive signal to the sound pressure signal of the sensing point (e2) and for the IM strategy is from the shaker drive signal to the sound pressure signal of the reflected plane wave in the cavity. The control results for the experiment are shown in Fig.17 (b), which agrees well with the theoretical results and validates the theoretical findings. The sound absorption coefficient with control is undulant and slightly lower than the theoretical results. This may be due to the

not very uniform cavity sound field, which is induced by the slight modal deformation of the backing panel with non-ideal simply supported boundary condition.

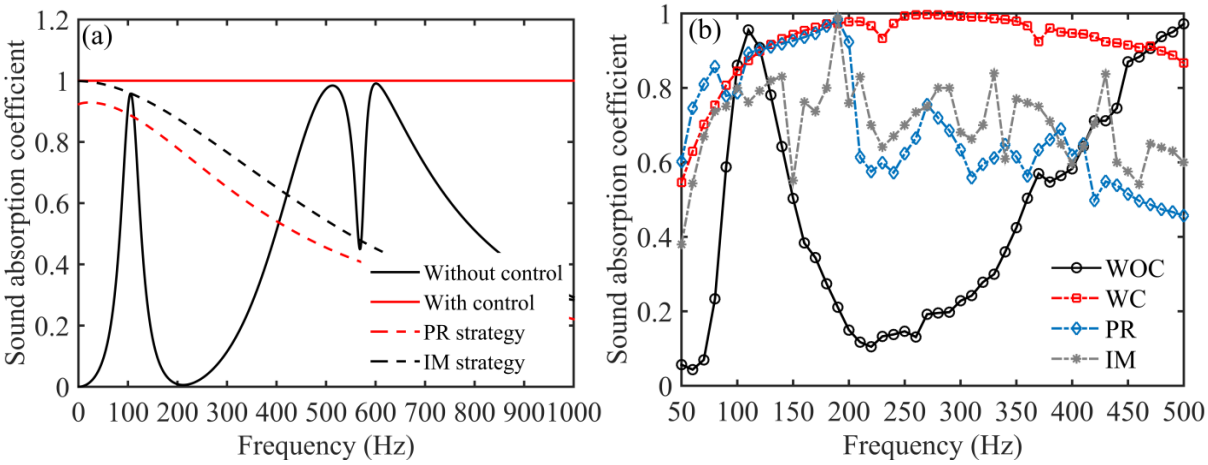

Fig.17. Control results for the PR and IM strategies: (a) theory, (b) experiment.

7. Conclusions

The performance of the SAC-AMPPA is investigated thoroughly in this research. The control effect and physical mechanism are analyzed in detail. Simplified error sensing strategy is constructed. Experiments are carried out to validate the theoretical findings. Conclusions obtained are summarized as follows.

(1) The control performance of the SAC-AMPPA is highly correlated with the size of the structure and the location of the point force. The optimal location of the point force is the center of the backing panel, which can gain the widest controllable bandwidth and the upper limit frequency is the resonant frequency of the (0,2,0) cavity mode. The small sized SAC-AMPPA is beneficial to obtain wide controllable bandwidth.

(2) The (odd, odd) panel mode excited-(0,0,0) cavity mode plays a key role in the improvement of sound absorption with control and also in the production of absorption peaks without control. Other high order cavity modes have no contribution to the improvement of sound absorption when the excitation frequency is lower than their resonance frequencies, and they even radiate sound energy to the outside of the SAC-AMPPA and have the opposite effect on the improvement of sound absorption above their resonant frequencies. This is the reason of appearing a different controllable upper limit cutoff frequency for different location of the point force.

(3) Since only the (0,0,0) cavity mode works with control, the PR and IM strategies are applicative for simplifying the error sensing strategy of the SAC-AMPPA. The approximate uniform cavity sound field is guaranteed with control for the small sized SAC-AMPPA with point force locating at the optimal position, which can gain good control effect.

Acknowledgments

This work was financially supported by the China Postdoctoral Science Foundation (Grant No. 2019M663821), the Fundamental Research Funds for the Central Universities (Grant No. 3102019HHZY030025), the Natural Science Basic Research Plan in Shaanxi Province of China (Grant No. 2018JQ1025), the National Natural Science Foundation of China (NSFC, Grant No. 51705421).

Appendix A

(1) The row vector $\mathbf{G}_1$ and $\mathbf{G}_2$, and the column vector $\mathbf{\Psi}$ can be expressed as,

$$\mathbf{G}_1 = [\frac{j\omega Z_{00}^r A_{00}}{\beta^{00}}(\mathbf{E}^{-1}\mathbf{D})^T\boldsymbol{\gamma}^{00},...\frac{j\omega Z_{uw}^r A_{uw}}{\beta^{uw}}(\mathbf{E}^{-1}\mathbf{D})^T\boldsymbol{\gamma}^{uw},...\frac{j\omega Z_{UW}^r A_{UW}}{\beta^{UW}}(\mathbf{E}^{-1}\mathbf{D})^T\boldsymbol{\gamma}^{UW}], \quad \text{(A1)}$$

$$\mathbf{G}_2 = [\frac{j\omega Z_{00}^r A_{00}}{\beta^{00}}(\mathbf{E}^{-1}\mathbf{Q})^T\boldsymbol{\gamma}^{00},...\frac{j\omega Z_{uw}^r A_{uw}}{\beta^{uw}}(\mathbf{E}^{-1}\mathbf{Q})^T\boldsymbol{\gamma}^{uw},...\frac{j\omega Z_{UW}^r A_{UW}}{\beta^{UW}}(\mathbf{E}^{-1}\mathbf{Q})^T\boldsymbol{\gamma}^{UW}], \quad \text{(A2)}$$

$$\mathbf{\Psi} = [\varphi_{00}(x,y),...\varphi_{uw}(x,y),...\varphi_{UW}(x,y)]^T. \quad \text{(A3)}$$

(2) The row vector $\mathbf{H}_1$ and $\mathbf{H}_2$ can be expressed as,

$$\mathbf{H}_1 = [\frac{j\omega A_{00}}{\beta^{00}}(\mathbf{E}^{-1}\mathbf{D})^T\boldsymbol{\gamma}^{00},...\frac{j\omega A_{uw}}{\beta^{uw}}(\mathbf{E}^{-1}\mathbf{D})^T\boldsymbol{\gamma}^{uw},...\frac{j\omega A_{UW}}{\beta^{UW}}(\mathbf{E}^{-1}\mathbf{D})^T\boldsymbol{\gamma}^{UW}], \quad \text{(A4)}$$

$$\mathbf{H}_2 = [\frac{j\omega A_{00}}{\beta^{00}}(\mathbf{E}^{-1}\mathbf{Q})^T\boldsymbol{\gamma}^{00},...\frac{j\omega A_{uw}}{\beta^{uw}}(\mathbf{E}^{-1}\mathbf{Q})^T\boldsymbol{\gamma}^{uw},...\frac{j\omega A_{UW}}{\beta^{UW}}(\mathbf{E}^{-1}\mathbf{Q})^T\boldsymbol{\gamma}^{UW}]. \quad \text{(A5)}$$

(3) The variables a_1, b_1, c_1 and d_1 are expressed as,

$$a_1 = \mathbf{G}_2\mathbf{\Omega}\mathbf{H}_2^H,\ b_1 = \mathbf{G}_2\mathbf{\Omega}\mathbf{H}_1^H + \mathbf{G}_2\mathbf{\Omega}_1(v_1^{rigid})^H,\ c_1 = \mathbf{G}_1\mathbf{\Omega}\mathbf{H}_2^H + \mathbf{\Omega}_1^T\mathbf{H}_2^H P_{rigid},$$

$$d_1 = \mathbf{G}_1\mathbf{\Omega}\mathbf{H}_1^H + \mathbf{G}_1\mathbf{\Omega}_1(v_1^{rigid})^H + \mathbf{\Omega}_1^T\mathbf{H}_1^H P_{rigid} + abP_{rigid}(v_1^{rigid})^H, \quad \text{(A6)}$$

where $\mathbf{\Omega} = \int_0^a\int_0^b \mathbf{\Psi}\mathbf{\Psi}^H \mathrm{d}x\mathrm{d}y$, $\mathbf{\Omega}_1 = \int_0^a\int_0^b \mathbf{\Psi}\mathrm{d}x\mathrm{d}y$.

Appendix B

The measured sound absorption coefficients of the empty tube used in the experiment with rigid end and open end are shown in Fig.B. There may be slight sound leakage at the end of the tube and at the joint of the tube, hence, the sound absorption coefficient of the empty tube with rigid end measured in the experiment is slightly larger than 0, as shown in Fig.B (a). The sound wave in the empty tube will encounter very soft boundary at the open end, which results that most of the incident plane wave at the open end will be reflected. Then, the sound absorption coefficient

of the empty tube with open end is also very small, as shown in Fig.B (b).

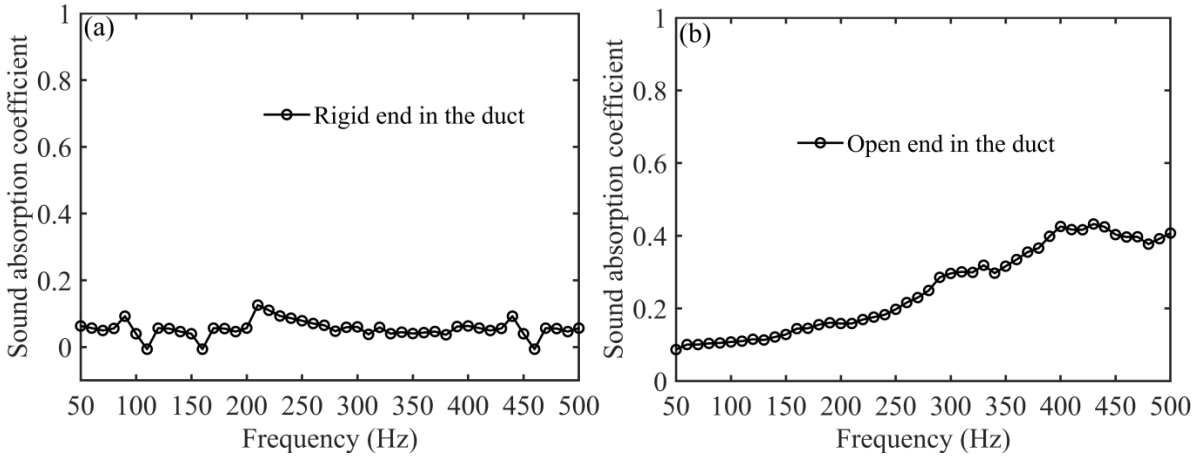

Fig.B (a) The sound absorption coefficient of the empty tube with rigid end, (b) the sound absorption coefficient of the empty tube with open end.

Appendix C

The amplitudes of the measured sound pressure at the measurement points P1 and P2 (the complex amplitude in frequency domain) with control are listed in Table C for each testing frequency (D-Case 1, D-Case 2, and D-Case 3).

Table C The amplitudes of the sound pressure at P1 and P2 with control

Frequency (Hz)	The amplitude of the sound pressure (Pa)					
	D-Case 1		D-Case 2		D-Case 3	
	P1	P2	P1	P2	P1	P2
50	0.55+0.54i	0.53+0.46i	0.04-0.03i	0.02-0.07i	-0.01-0.03i	-0.03-0.03i
60	-0.30+0.24i	-0.26+0.25i	0.15-0.07i	0.09-0.20i	-0.08+0.02i	-0.07+0.08i
70	-0.08-0.86i	-0.16-0.85i	-0.19+0.34i	0.12+0.47i	0.14+0.14i	0.26+0.02i
80	-0.78+0.57i	-0.72+0.75i	0.15+0.68i	0.67+0.43i	-0.04-0.35i	-0.28-0.27i
90	0.85+0.91i	1.03+0.61i	-0.15+0.95i	0.62+0.85i	0.27-0.35i	-0.04-0.49i
100	1.03+1.54i	1.17+1.27i	1.16+0.05i	0.88-0.83i	0.50-0.17i	0.28-0.50i
110	1.40+1.00i	1.52+0.86i	-1.08+0.68i	-0.25+1.25i	0.29-0.52i	-0.15-0.59i
120	-0.03-0.17i	-0.10-0.20i	0.76+1.14i	1.29+0.22i	0.34+0.51i	0.61+0.13i
130	0.02+0.17i	0.08+0.17i	-0.57+1.29i	0.52+1.20i	-0.61+0.20i	-0.28+0.56i

140	-0.05+1.62i	0.004+0.14i	1.00-1.48i	-0.35-1.57i	-0.31-0.56i	-0.59-0.17i
150	-0.13-0.06i	-0.14-0.01i	0.47+0.11i	0.36-0.24i	-0.41-0.46i	-0.57-0.01i
160	0.20+0.08i	0.14+0.01i	-0.41+0.19i	-0.12+0.37i	-0.41-0.41i	-0.54-0.01i
170	-0.11+0.04i	-0.11+0.10i	-0.32+0.22i	-0.05+0.34i	-0.49+0.17i	-0.21+0.44i
180	-0.10+0.04i	-0.09+0.10i	-0.33+0.12i	-0.12+0.28i	-0.12-0.44i	-0.36-0.20i
190	-0.17+0.16i	-0.18+0.26i	-0.12+0.28i	-0.26+0.10i	0.40+0.12i	0.33-0.20i
200	0.08+0.54i	0.39+0.59i	0.01+0.32i	0.19+0.19i	-1.28-0.96i	-1.39+0.27i
210	0.25-0.07i	0.22-0.23i	-0.28+0.01i	-0.14+0.18i	0.42+0.53i	0.61+0.03i
220	-0.13+0.02i	-0.20+0.17i	-0.15-0.30i	-0.25-0.06i	-0.11-0.61i	-0.48-0.26i
230	-0.04+0.08i	0.01+0.11i	0.58+0.19i	0.36-0.19i	-0.52+0.06i	-0.12+0.36i
240	-0.03+0.01i	-0.00+0.06i	0.75-1.54i	-0.35-1.48i	-0.43+0.42i	0.04+0.49i
250	0.06-0.09i	-0.04-0.12i	0.14+1.43i	1.09+0.88i	-0.38-0.31i	-0.31+0.17i
260	0.12+0.05i	0.13-0.08i	-0.77+0.48i	-0.15+0.90i	0.05-0.56i	-0.35-0.31i
270	0.03-0.02i	-0.01-0.04i	0.72-0.16i	0.33-0.68i	0.33-0.95i	-0.46-0.67i
280	-0.03+0.08i	0.05+0.07i	-0.67-0.01i	-0.43+0.56i	0.26-0.96i	-0.51-0.67i
290	0.05+0.07i	-0.02+0.08i	-0.31-0.52i	-0.65-0.05i	0.26-0.96i	0.43-0.61i
300	0.05-0.01i	0.00-0.06i	0.42+0.34i	0.58-0.19i	-0.51-0.18i	-0.47+0.35i
310	-0.00-0.05i	-0.06-0.01i	0.47-0.13i	0.15-0.55i	-0.45-0.19i	-0.50+0.26i
320	0.03-0.05i	-0.05-0.04i	0.42+0.21i	0.45-0.31i	0.20+0.27i	0.51-0.03i
330	-0.06-0.02i	-0.04+0.06i	0.40-0.14i	0.05-0.52i	0.24+0.23i	0.45-0.21i
340	-0.06-0.02i	-0.03+0.07i	0.33+0.23i	0.43-0.26i	-0.08+0.07i	0.05+0.15i
350	0.01+0.07i	0.08-0.01i	-0.34-0.17i	-0.36+0.33i	0.05-0.07i	-0.03-0.15i
360	0.11-0.02i	-0.02-0.14i	-0.24-0.26i	-0.46+0.19i	-0.09-0.02i	-0.09+0.13i

370	-0.05-0.13i	-0.18+0.08i	0.26+0.17i	0.42-0.25i	0.15-0.08i	-0.04-0.32i
380	0.09+0.09i	0.12-0.15i	-0.03-0.36i	-0.54-0.03i	-0.04-0.23i	-0.43-0.00i
390	0.05-0.07i	-0.12-0.06i	-0.01-0.37i	-0.57-0.01i	0.07-0.24i	-0.44-0.15i
400	0.002+0.09i	0.14-0.02i	-0.39-0.08i	-0.08+0.61i	-0.30-0.04i	-0.01+0.49i
410	0.07+0.03i	0.04-0.13i	-0.40-0.08i	-0.04+0.62i	-0.28+0.15i	0.34+0.39i
420	0.07+0.001i	-0.005-0.14i	-0.36+0.19i	0.41+0.48i	-0.14-0.27i	-0.38+0.34i
430	0.09-0.03i	0.008-0.05i	0.04+0.39i	0.55-0.26i	0.28+0.03i	-0.08-0.45i
440	0.33+0.05i	0.24-0.20i	-0.34-0.11i	0.07+0.53i	-0.26-0.06i	-0.03+0.39i
450	0.32-0.15i	-0.01-0.37i	-0.32-0.02i	0.20+0.42i	0.19+0.15i	0.10-0.33i
460	-0.32+0.10i	0.08+0.32i	0.24+0.16i	0.00-0.41i	-0.06-0.20i	-0.18+0.24i
470	-0.13-0.25i	-0.18+0.12i	0.16-0.22i	-0.37-0.00i	0.19+0.02i	-0.14-0.24i
480	0.36-0.02i	-0.01-0.18i	-0.01-0.25i	-0.26+0.22i	0.16-0.09i	-0.23-0.07i
490	-0.36+0.43i	0.05+0.40i	0.07+0.22i	0.14-0.27i	0.02+0.18i	0.13-0.18i
500	0.22-0.12i	-0.10-0.27i	0.20-0.10i	-0.28-0.07i	-0.16-0.0i	-0.08+0.20i

References

[1] Y. Mao, C. Fan, Z. Zhang, S. Song, C. Xu, Control of noise generated from centrifugal refrigeration compressor, Mech. Syst. Signal Pr. 152 (2021) 1-18. https://doi.org/10.1016/j.ymssp.2020.107466

[2] Y. Tang, W. He, F. Xin, T. Lu, Nonlinear sound absorption of ultralight hybrid-cored sandwich panels, Mech. Syst. Signal Pr. 135 (2020) 1-11. https://doi.org/10.1016/j.ymssp.2019.106428

[3] D. Maa, Potential of microperforated panel absorber, J. Acoust. Soc. Am. 104 (1998) 2861-2866. https://doi.org/10.1121/1.423870

[4] Z.M. Zhang, X.T. Gu, The theoretical and application study on a double layer microperforated sound absorption structure, J. Sound Vib. 215 (1998) 399-405. https://doi.org/10.1006/jsvi.1997.1693

[5] K. Sakagami, T. Nakamori, M. Morimoto, M. Yairi, Double-leaf microperforated panel space absorbers: A revised theory and detailed analysis, Appl. Acoust. 70 (2009) 703-709. https://doi.org/10.1016/j.apacoust.2008. 09.004

[6] K. Sakagami, K. Matsutani, M. Morimoto, Sound absorption of a double-leaf micro-perforated panel with an air-back cavity and a rigid-back wall: Detailed analysis with a Helmholtz-Kirchhoff integral formulation, Appl. Acoust. 71 (2010) 411-417. https://doi.org/10.1016/j.apacoust.2009.11.014

[7] D.H. Lee, Y.P. Kwon, Estimation of the absorption performance of multiple layer perforated panel systems by transfer matrix method, J. Sound Vib. 278 (2004) 847-860. https://doi.org/10.1016/j.jsv.2003.10.017

[8] H. Ruiz, P. Cobo, F. Jacobsen, Optimization of multiple-layer microperforated panels by simulated annealing, Appl. Acoust. 72 (2011) 772-776. https://doi.org/10.1016/j.apacoust.2011.04.010

[9] R.B. Tayong, J.A. Manyo, E. Siryabe, G.E. Ntamack, On the simultaneous inversion of micro-perforated panels' parameters: Application to single and double air-cavity backed systems, J. Acoust. Soc. Am. 143 (2018) 2279-2288. https://doi.org/10.1121/1.5032312

[10] C. Wang, L. Huang, On the acoustic properties of parallel arrangement of multiple micro-perforated panel absorbers with different cavity depths, J. Acoust. Soc. Am. 130 (2011) 208-218. https://doi.org/10.1121/1.3596459

[11] C. Wang, L. Huang, Y. Zhang, Oblique incidence sound absorption of parallel arrangement of multiple micro-perforated panel absorbers in a periodic pattern, J. Sound Vib. 333 (2014) 6828-6842. https://doi.org/10.1016/j.jsv. 2014.08.009

[12] C.Q. Wang, L. Cheng, J. Pan, G.H. Yu, Sound absorption of a micro-perforated panel backed by an irregular-shaped cavity, J. Acoust. Soc. Am. 127 (2010) 238-246. https://doi.org/10.1121/1.3257590

[13] C. Yang, L. Cheng, J. Pan, Absorption of oblique incidence sound by a finite micro-perforated panel absorber, J. Acoust. Soc. Am. 133 (2013) 201-209. https://doi.org/10.1121/1.4768869

[14] T. Bravo, C. Maury, Sound attenuation and absorption by micro-perforated panels backed by anisotropic fibrous materials: Theoretical and experimental study, J. Sound Vib. 425 (2018) 189-207. https://doi.org/10.1016/j.jsv.2018.04. 006

[15] Y.J. Qian, D.Y. Kong, S.M. Liu, S.M. Sun, Z. Zhao, Investigation on micro-perforated panel absorber with ultra-microperforations, Appl. Acoust. 74 (2013) 931-935. https://doi.org/10.1016/j.apacoust.2013.01.009

[16] X. Gai, X. Li, B. Zhang, T. Xing, J. Zhao, Z. Ma, Experimental study on sound absorption performance of microperforated panel with membrane cell, Appl. Acoust. 110 (2016) 241-247. https://doi.org/10.1016/j.apacoust.2016.03. 034

[17] X. Gai, T. Xing, X. Li, B. Zhang, Sound absorption properties of microperforated panel

with membrane cell and mass blocks composite structure, Appl. Acoust. 137 (2018) 98-107. https://doi.org/10.1016/j.apacoust.2018.03. 013

[18] S.W. Ren, L. Belle, C. Claeys, F. X. Xin, T.J. Lu, E. Deckers, W. Desmet, Improvement of the sound absorption of flexible micro-perforated panels by local resonances, Mech. Syst. Signal Pr. 117 (2019) 138-156. https://doi.org/10.1016/j.ymssp.2018.07.046

[19] X. Gai, T. Xing, X. Li, B. Zhang, W. Wang, Sound absorption of microperforated panel mounted with Helmholtz resonators, Appl. Acoust. 114 (2016) 260-265. https://doi.org/10.1016/j.apacoust.2016.08.001

[20] M. Toyoda, D. Takahashi, Sound transmission through a microperforated-panel structure with subdivided air cavities, J. Acoust. Soc. Am. 124 (2008) 3594-3603. https://doi.org/10.1121/1.3001711

[21] J. Liu, D.W. Herrin, Enhancing micro-perforated panel attenuation by partitioning the adjoining cavity, Appl. Acoust. 71 (2010) 120-127. https://doi.org/10.1016/j.apacoust.2009.07.016

[22] S. Xie, D. Wang, Z. Feng, S. Yang, Sound absorption of microperforated honeycomb metasurface panels with a combination of multiple orifice diameters, Appl. Acoust. 158 (2020) 1-8. doi.org/10.1016/j.apacoust.2019.107046

[23] S. Park, Acoustic properties of micro-perforated panel absorbers backed by Helmholtz resonators for the improvement of low-frequency sound absorption, J. Sound Vib. 332 (2013) 4895-4911. https://doi.org/10.1016/j.jsv.2013.04.029

[24] X.H. Duan, H.Q. Wang, Z.B. Li, L.K. Zhu, R. Chen, D.Y. Kong, Z. Zhao, Sound absorption of a flexible micro-perforated panel absorber based on PVDF piezoelectric film, Appl. Acoust. 88 (2015) 84-89. https://doi.org /10.1016/j.apacoust.2014.08.009

[25] X. Zhao, X. Fan, Enhancing low frequency sound absorption of micro-perforated panel absorbers by using mechanical impedance plates, Appl. Acoust. 88 (2015) 123-128. https://doi.org/10.1016/j.apacoust.2014.08.015

[26] J. Tao, R. Jing, X. Qiu, Sound absorption of a finite micro-perforated panel backed by a shunted loudspeaker, J. Acoust. Soc. Am. 135 (2014) 231-238. https://doi.org/10.1121/1.4836215

[27] C. Wang, X. Liu, Investigation of the acoustic properties of corrugated micro-perforated panel backed by a rigid wall, Mech. Syst. Signal Pr. 140 (2020) 1-17. https://doi.org/10.1016/j.ymssp.2020.106699

[28] P.A. Nelson, S.J. Elliott, Active control of sound. London: Academic Press, 1991.

[29] X. Li, Y. Chen, R. Zhu, G. Huang, An active meta-layer for optimal flexural wave absorption and cloaking, Mech. Syst. Signal Pr. 149 (2021) 107324.

https://doi.org/10.1016/j.ymssp.2020.107324
[30] Y. Chen, X. Li, H. Nassar, G. Hu, G. Huang, A programmable metasurface for real time control of broadband elastic rays, Smart Mater. Struct. 27 (2018) 115011. https://doi.org/10.1088/1361-665X/aae27b
[31] Y. Chen, X. Li, C. Scheibner, V. Vitelli, G. Huang, Realization of active metamaterials with odd micropolar elasticity, Nat. Commun. 12 (2021) 5935. https://doi.org/10.1038/s41467-021-26034-z
[32] P. Cobo, J. Pfretzschner, M. Cuesta, D.K. Anthony, Hybrid passive-active absorption using microperforated panels, J. Acoust. Soc. Am. 116 (2004) 2118-2125. https://doi.org/10.1121/1.1786831
[33] P. Cobo, M. Cuesta, Hybrid passive-active absorption of a microperforated panel in free filed conditions, J. Acoust. Soc. Am. 121 (2007) EL251-EL255. https://doi.org/10.1121/1.2739112
[34] P. Cobo, M. Cuesta, Measuring hybrid passive-active sound absorption of a microperforated liner at oblique incidence, J. Acoust. Soc. Am. 125 (2009) 185-190. https://doi.org/10.1121/1.3026328
[35] X. Ma, K. Chen, L. Wang, Y. Liu, S. Ding, Active control of low frequency sound absorption of large sized micro-perforated panel absorber by using point source, Appl. Acoust. 185 (2022) 1-13. https://doi.org/10.1016/j.apacoust.2021.108424
[36] K. Yang, W. Tong, L. Lin, D. Yurchenko, J. Wang, Active vibration isolation performance of the bistable nonlinear electromagnetic actuator with the elastic boundary, J. Sound Vib. (2021) 1-15. https://doi.org/10.1016/j.jsv.2021.116588
[37] K. Yang, A. Abdelkefi, X. Li, Y. Mao, L. Dai, J. Wang, Stochastic analysis of a galloping-random wind energy harvesting performance on a buoy platform, Energ. Convers. Manage. 238 (2021) 114174. https://doi.org/10.1016/j.enconman.2021.114174
[38] J. Wang, W. Zhao, Z. Su, G. Zhang, P. Li, D. Yurchenko, Enhancing vortex-induced vibrations of a cylinder with rod attachments for hydrokinetic power generation, Mech. Syst. Signal Pr. 145 (2020) 106912(1-16). https://doi.org/10.1016/j.ymssp.2020.106912
[39] J. Wang, S. Sun, L. Tang, G. Hu, J. Liang, On the use of metasurface for Vortex-Induced vibration suppression or energy harvesting, Energ. Convers. Manage. 235 (2021) 113991. https://doi.org/10.1016/j.enconman.2021.113991
[40] X. Ma, K. Chen, L. Wang, Y. Liu, Error sensing strategy for active control of low-frequency sound absorption of micro-perforated panel absorber by using a point force controlled thin plate, Shock Vib. 2021 (2021) 1-16. https://doi.org/10.1155/2021/6691505
[41] Y.Y. Lee, E.W.M. Lee, C.F. Ng, Sound absorption of a finite flexible micro-perforated

panel backed by an air cavity, J. Sound Vib. 287 (2005) 227-243. https://doi.org/10.1016/j.jsv.2004.11.024

[42] T. Bravo, C. Maury, C. Pinhede, Vibroacoustic properties of thin micro-perforated panel absorbers, J. Acoust. Soc. Am. 132 (2012) 789-798. https://doi.org/10.1121/1.4733555

[43] T. Bravo, C. Maury, C. Pinhede, Sound absorption and transmission through flexible micro-perforated panels backed by an air layer and a thin plate, J. Acoust. Soc. Am. 131 (2012) 3853-3863. https://doi.org/10.1121/1.3701987

[44] T. Bravo, C. Maury, C. Pinhede, Enhancing sound absorption and transmission through flexible multi-layer micro-perforated structures, J. Acoust. Soc. Am. 134 (2013) 3663-3673. https://doi.org/10.1121/1.4821215